Exploring the mechanical properties of two-dimensional carbon-nitride polymer nanocomposites by molecular dynamics simulations

Qinghua Zhang, Bohayra Mortazavi, Xiaoying Zhuang, Fadi Aldakheel

MMDM (Material Modeling and Damage Mechanics) Lab

Exploring the mechanical properties of two-dimensional carbon-nitride polymer nanocomposites by molecular dynamics simulations

Qinghua Zhang[a], Bohayra Mortazavi[b], Xiaoying Zhuang[b,c], Fadi Aldakheel[a,d,1]

[a]Institute of Continuum Mechanics, Department of Mechanical Engineering, Leibniz Universität Hannover, An der Universität 1, 30823 Garbsen, Germany.

[b]Chair of Computational Science and Simulation Technology, Institute of Photonics, Department of Mathematics and Physics, Leibniz Universität Hannover, Appelstraße 11, 30167 Hannover, Germany.

[c]College of Civil Engineering, Department of Geotechnical Engineering, Tongji University, 1239 Siping Road Shanghai, China.

[d]Zienkiewicz Centre for Computational Engineering, Faculty of Science and Engineering, Swansea University, Bay Campus, SA1 8EN, UK

Abstract

The enhancement of mechanical properties of polymeric materials by the addition of strong nanomaterials is currently among the most appealing routes for the application of polymers in structural components and nanoelectronics. Carbon-nitride nanomembranes have attracted remarkable attention due to their outstanding physical properties in recent years. In this study, the role of graphene (GN) and various carbon-nitride (C_xN_y) nanosheets on the mechanical reinforcement of P3HT polymer nanocomposites is systematically investigated by conducting extensive molecular dynamics (MD) simulations. We first elaborately examine the mechanical responses of pristine nanosheets. Next, we construct large atomistic models of polymer nanocomposites to examine the effective mechanical properties as a function of nanofillers content. To this end, the interfacial strength and cohesive zone properties between various nanosheets and the polymer are investigated. With the aid of constructed models, we explore the underlying mechanisms of mechanical reinforcement and formation of initial crack and its correlation with interface strength between nanosheets and polymer. Furthermore, the effects of nanoporosity in the nanomembranes lattice and the resulting interfacial strength and mechanical response are discussed. Acquired findings provide a useful vision for understanding the mechanical/failure responses of polymer nanocomposites reinforced with carbon-nitride nanosheets.

Keywords: *Mechanical Properties; Molecular Dynamics; Graphitic Carbon Nitride Nanosheet; Material modeling; Failure Behavior; Polymer-matrix composites (PMCs); Computational modeling.*

1. Introduction

Organic semiconductor polymers play an important role in the development of various components and devices through the years due to their flexibility, portability, and lower possible manufacturing costs [1,2]. Among several polymeric semiconductors, poly(3-octylthiophene) (P3HT) is one of the most prevalent semiconducting polymers in research [3–7] and optoelectronic devices development [8]. Compared to conventional electric and thermal insulating polymers, P3HT has good electric properties, and conversion efficiency [9–11]. Recently, a work by Yanfei et al indicates that P3HT has not only a good electrical property but also an excellent thermal conductivity while conjugated with other polymers [12]. However, the mechanical property of the P3HT is more brittle compared to the conventional polymer, since the rupture of the material occurs at a deformation of 9±1.2% [13] during the tensile. In this regard, P3OT, P3DDT are from the same family polymers with a strain of 65.24±2.5%, 47±3.1% for an initial fracture in tensile, respectively [14]. This poor mechanical property restricted the development and application of P3HT in many fields. To address such an issue, the conventional method is to disperse conductive or mechanical reinforced particles in an elastic matrix [15] and maximize the interaction area between filler and matrix by using smaller size particle fillers [16]. So that the material physical properties can be improved. On behalf of this, the physical properties and the topology of reinforcements play a key role in enhancing the nanocomposite's mechanical and thermal properties. Consequently, materials with excellent mechanical and thermal conductivity properties like graphene or carbon nitride monolayers were considered as reinforcements, as outlined in [17,18]. Since those monolayers possess not only

---

[1] **Corresponding author: aldakheel@ikm.uni-hannover.de**

extraordinary mechanical properties but also the most efficient interaction areas for enhancement constitution among several topologies.

Recently, numerous reports have shown that some carbonates and nitrides monolayers possess high mechanical and thermal conductivity. Two-dimensional (like graphene and carbon-nitride) nanomaterials are regarded as one of the most attractive research topics in a wide field by using a numerical simulation combined with experiments [19–24]. Graphene possesses high electrical [25], thermal conductivity [26], and mechanical properties since the exploration from 2004. A work from Lee et al. reveals that the intrinsic strength of GN can be investigated 130±10 GPa in the experiment [27]. With the consideration of such extraordinary properties, graphene has been used as a reinforcement in many polymeric matrices to improve rigidity or thermal conductivity [28]. In the industries, GN has been widely used for development of energy storage devices [29,30], thermal management [31,32], supercapacitor [33,34], sensor [35,36], and stiffening [37,38]. Several mechanical and thermal conductivity of the graphene reinforced composites indicates that graphene is a unique nanofiber for materials physical properties enhancement [39].

On the other hand, C_3N carbon nitride as a new semiconductor has excellent mechanical properties. The pristine C_3N tensile strength can reach 35.2 GPa.nm which is much close to defect-free graphene as outlined in [40]. From the perspective of stability, the C_3N was found to be stable at 550℃, which is regarded as more stable than GN with stability to 480℃ [41]. Recently, Weiming et al reveal that C_3N possesses better property for load transfer dues to a higher capacity of hydrogen bonding of the nanosheet at the interface [42]. From the experiments' point of view, the novel two-dimensional C_3N_5 semiconductor was successfully realized by two s-heptazine units connected with azo-linkage [43] after a few theoretical investigations by molecular dynamics. This enables theoretical carbon nitride materials to be fabricated. It also demonstrates that the exploration of nanomaterials by molecular dynamics is reliable in nanomaterials investigation. All above superior reinforcing properties of carbon-nitride and GN exhibit a big potential to satisfy various requirements from the aerospace and electric vehicle industry by enhancing conventional materials' fundamental and functional properties. However, few reports are related to the exploration of the mechanical properties of carbon nitride (C_xN_y) as reinforcement inside an impressive semiconductor matrix (P3HT). From the perspective of reinforced composite, several works indicate that GN reinforced P3HT composite possesses 36 times enhancement mobility [44], and MoS_2/P3HT composite exhibits extraordinary high cycle stability in [3]. But an effective method to explore mechanical properties between types of GN, C_xN_y, and matrix with the experiment is very hard. Moreover, the experiment is hard to carry out for such tiny scale-like 2D materials with only a few-layer thicknesses. Additionally, the non-bond interaction of the interface is difficult to measure through experiments, especially smaller than microscale. For those issues, the MD method provides an access to investigate those enhanced materials by the numeric method in theory implementation [4]. MD can save a great deal of time and cost in research, also get good convergence in wide fields. From the perspective of material designing, the conventional composite mechanical properties study focuses heavily on enhancement comparison rather than the design to fracture mechanism investigation. In this contribution, we provide a multi-dimension composite mechanical properties investigation base on molecular dynamics. Moreover, by fracture analysis of the composite and reinforcements, we proposed two types of enhancements named active and passive enhancement for carbon-nitride reinforcements. Then the interfacial strength between reinforcement and matrix was investigated by the cohesive model. By further studying the interaction of interfaces, this study could significantly explain the root of the initial crack occurring during composite uniaxial tensile.

Therefore, to better understand the mechanical properties and the fracture mechanism of the Graphene (GN), carbon-nitride (C_xN_y) reinforced P3HT nanocomposite, the basic mechanical properties of fillers and matrices need to be explored and valid. Firstly, the uniaxial tensile of the two-dimensional reinforcement was performed to obtain the fundamental mechanical response of the filler (Graphene, C_xN_y) at different strain rates and deformation orientations. Second, the basic mechanical property and stability of the matrices were tested to find out the most stable matrix. Then, 5%, 10%, and 15% reinforced volumetric fractions composite will be constructed by Amorphous Cell modules of Materials Studio (MS) and evaluated by LAMMPS. Finally, the interface between the reinforcements and the matrix will be explored by the cohesive model to predict the relationship between traction and separation for the monolayer.

2. Computational methods

As depicted in Fig.1, the reinforcement atomic structure of the 2D nanosheet consists of GN, C_2N, C_3N, C_3N_4, C_6N_6, and C_7N_6. From Fig.1 (a) to (f), it was shown that the brown atoms represent carbon atoms; the gray atoms represent nitrogen atoms. In Fig.1 (g), a basic monomer of the P3HT matrix was illustrated the branched-chain is $-C_6H_{13}$. In this study, a pure P3HT model was built with a cubic size 69.5x69.5x69.5 Å and a predefined density of 1.1 *g/cm³*. Every chain has 45 monomers. This polymer cubic cell has 22700 atoms and 100 polymer chains, as shown in Fig.1 (g), a geometry optimization was taken for the model under fine quality, within the control of the SMART algorithm. The van der Waals (vdW) interaction is formulated by Lennard-Jones 9-6 potential with a predefined cutoff of 15.5 Å (very fine), and the Columbic interaction can be described by the *Ewald* simulation method with an accuracy of 1.0e-4 *kcal/mol*. The COMPASS forcefield was carried out for the atomic interaction potential [45]. Moreover, the feasibility of COMPASS forcefield for modeling carbon-based composites has been well proven in [46].
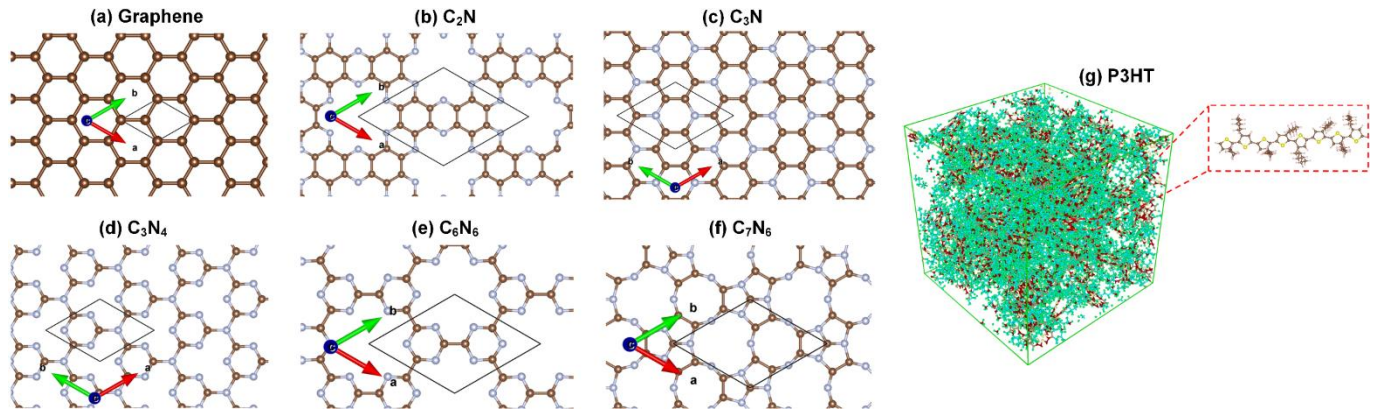
Fig.1, Atomic structure of Graphene(GN), carbon nitride monolayers, and P3HT structures in VESTA [47]; (g) is the pure P3HT polymer and zoom of part of a polymer chain from the polymer matrix illustrated using the OVITO [48] package.

In this section, *Tersoff* potential was used for formulating atomic interactions of graphene [49,50]. The optimized *Tersoff* potential was used to describe the bond interaction which was proposed by Lindsay and Broido for the formulation of the carbon-carbon atom interactions [51]. The potential parameters of the carbon-nitrogen interactions were used from the work of Kinacl [52]. The accuracy of the predictions derived from the MD simulations strongly correlates to the appropriate selection of the potential to define the atomic interactions, since the potential plays a key role in the accuracy calculation during the simulation. Besides, the optimized *Tersoff* potential is the most accurate potential for molecular dynamics simulation of the mechanical and thermal transport along with *sp2* carbon structure, as documented in [53]. Since the phonon dispersion curves of graphite were reproduced by employing Tersoff potential which is in close agreement with experimental measurements. Nevertheless, as discussed in our earlier study, the cutoff distance between C-C atoms was changed to 0.20 and 0.21 nm to remove the unphysical strain hardening in the stress-strain relation of graphene [54].

During uniaxial tensile of the polymer matrix (P3HT) and enhanced nanocomposite, a second-generation force field was used to describe the bond interaction [55]. It is worth mentioning that a hybrid potential was used to define the pair style. During the uniaxial tensile of C_xN_y/P3HT composite, an interaction of reinforcement can be formulated by *Tersoff* potential file which was created by Cem Sevik et al [52]. In terms of the interaction between the reinforcements (GN, C_xN_y) and the matrix, a conventional Lennard-Jones 9-6 potential was adopted to characterize the interatomic interaction among several atoms. From the perspective of classic molecular dynamics, the total energy consists of composite energy ($E_{composite}$), matrix energy (E_{matrxi}), reinforcement energy ($E_{reinforcement}$). The relationship is presented in formula (1).

$$E_{composite} = E_{reinforcement} + E_{matrix} + E_{interface} \qquad (1)$$

During the uniaxial tensile of the 2D nanosheet, a rectangular super-cell (about 146.0x71.8 Å) with 3822 atoms was constructed (see Fig.2(a)). It is worthwhile to mention that the output data will fluctuate much stronger when the construction with few numbers of atoms. Besides, Graphene and C_xN_y are presented with two major orientations, named armchair and zigzag directions as depicted in Fig.2(a). In this study, we explored the mechanical properties

of Graphene and C_xN_y monolayer with both armchair and zigzag orientations. A molecular dynamics method was carried in the simulation by LAMMPS (Large-scale Atomic/Molecular Massively Parallel Simulator) open-source package [56]. Reinforcements uniaxial tensile were taken place in a non-periodic boundary condition along the Z normal direction. Moreover, to ensure accurate uniaxial loading conditions, the automatically adjusted stress along with the perpendicular loading direction will be negligible by the NPT ensemble [40]. To avoid the dramatic stretching or void caused by loading, the atomic positions were rescaled as the applied loading changes in the simulation box length [40]. And the time increment and pair style were defined as 0.5 *fs* with *metal* unit and *Tersoff*, respectively. Next, a Gaussian distributed initial velocity was used to initialize the structure before the simulation. Then a cooling procedure was carried out for the structure from 500K to 300K by Nose Hoover barostat and thermostat (NPT) method for 30 *ps*. Besides, an equilibrium process should be taken for the structure within the target temperature (300K) for 30 ps in an NPT ensemble. Next, several constant strain rates ($2.0 \times 10^8 s^{-1}$, $6.0 \times 10^8 s^{-1}$, $2.0 \times 10^9 s^{-1}$, and $6.0 \times 10^9 s^{-1}$) were carried out during the reinforcement uniaxial test in NPT ensemble. Every 1 *ps*, the virial stress [57,58] was averaged 2 times to output the engineering stress-strain response. The virial stress (σ_{virial}) is bridging the atomic scale to the continuum scale by calculating the local or atomic level stress in molecular dynamics calculations, as indicated in [59], which can be formulated as follows:

$$\sigma_{virial} = \frac{1}{\Omega} \sum_{i \in \Omega} \left(-m_i \cdot \dot{u}_i \otimes \dot{u}_i + \frac{1}{2} \sum_{i \neq j} X_{ij} \otimes F_{ij} \right)$$

where Ω is the total volume; m_i, u_i, and X_i represents mass, position, and displacement of atom i, respectively; $\dot{u}_i = du_i/dt$ is the velocity; $X_{ij} = X_j - X_i$; $\otimes$ represents the dyadic product of two tensors; F_{ij} is the interatomic force between two atoms. When the stress is evaluated by the surface volume without considering the thickness of the monolayer, the stress unit will be attached by thickness as GPa.nm.

$$F_{ij} = \frac{\partial \varphi(x_{ij})}{\partial x_{ij}} \frac{X_{ij}}{x_{ij}}$$

Here, $x_{ij} = |X_{ij}|$, it is the distance between two atoms; $\varphi(x_{ij})$ is the interatomic potential that can be found in detailed parameters in *tersoff* potential file for the monolayer; the COMPASS or PCFF [55] force field for the polymer; the non-bond potential (van der Waals) for the interface zone.
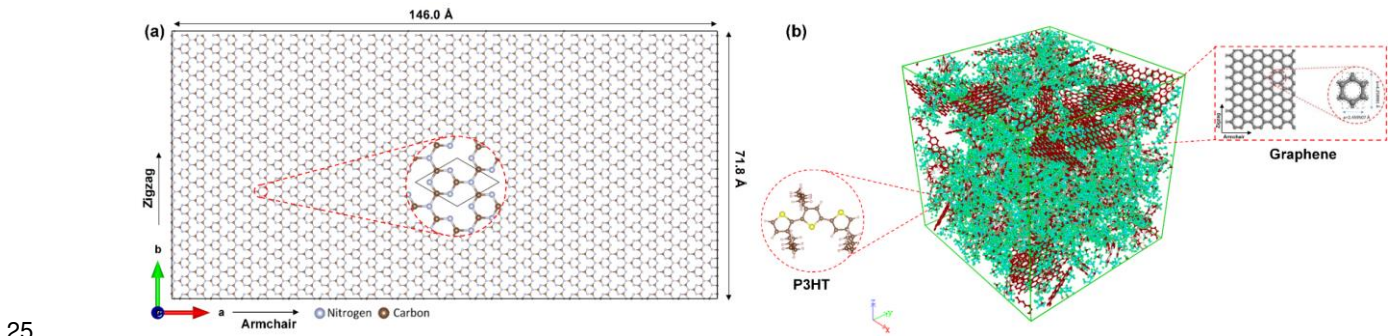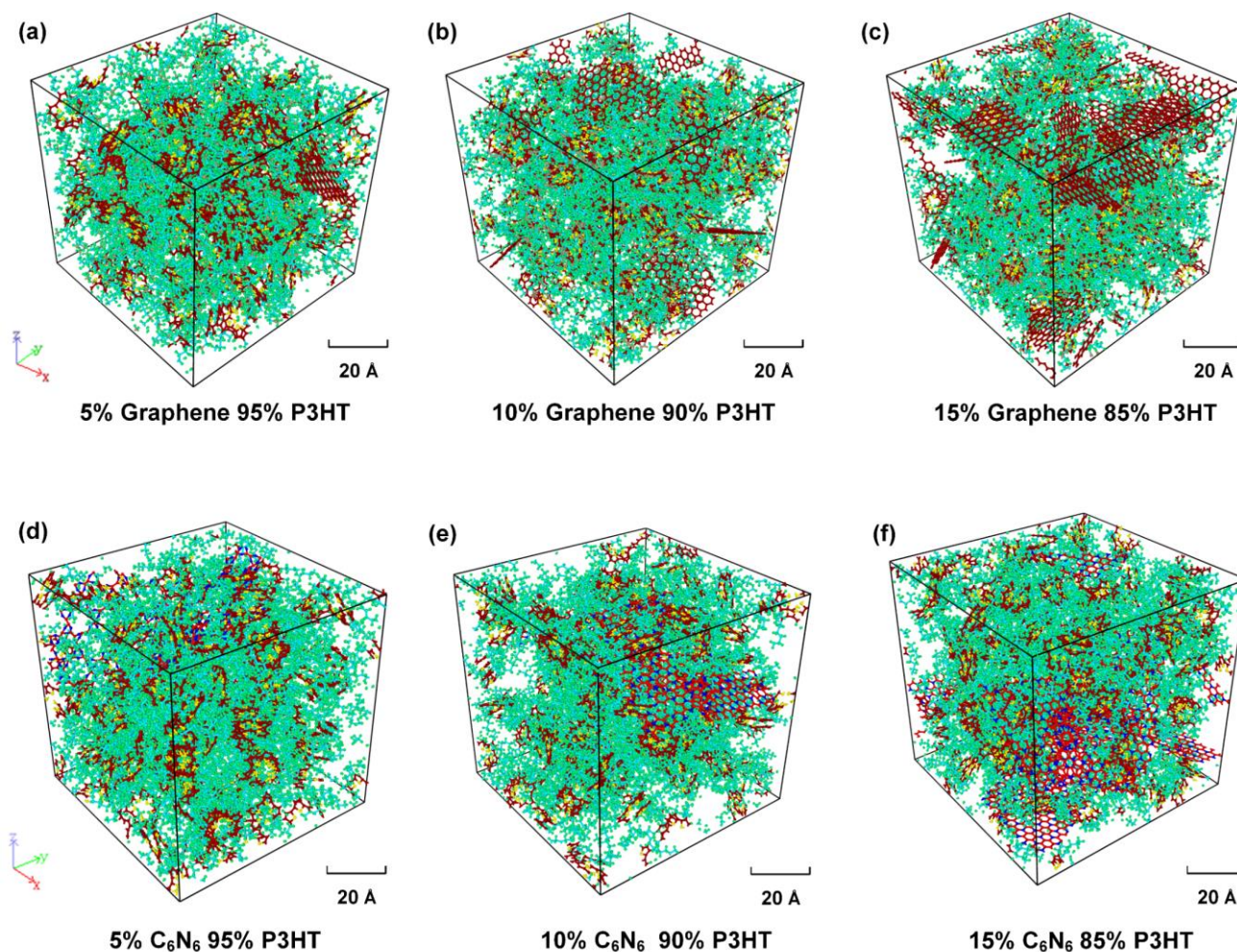

Fig.2, (a) C_3N_4 reinforcement uniaxial tensile model with 3822 atoms, with cell size 146.0x71.8 Å in VESTA [47], here is one of the reinforcements monolayer among several monolayers; the zoom figure is the basic lattice structure; (b) schematic illustration of the structure of 15% graphene 85% P3HT nanocomposite, the left zoomed graph is part of polymer chains and the unit, the right graph is the reinforcement monolayer and unit, others are the amorphous P3HT polymer.

During the P3HT uniaxial tensile, the calculation accuracy was defined with 1.0e-4 *kcal/mol* by the *Ewald* method; the cutoff was defined as 15.5 Å in 300K. After a geometry optimization was taken for the model in MS, the basic coordinates and force field parameters were converted to generalize data file in LAMMPS. 5 heating rates (1.41, 2.83, 5.67, 11.34, and 22.68 *K/ps*) were carried out for the density test. Furthermore, to get the most stable matrix for our composites, we have also compared different polymers (PT, P3OT). Finally, with the consideration of many application fields and excellent physical properties of P3HT, it was chosen as a composite matrix to tensile at 300K for 4 constant strain rates ($2.0 \times 10^9 s^{-1}$, $4.0 \times 10^9 s^{-1}$, $2.0 \times 10^{10} s^{-1}$, $4.0 \times 10^{10} s^{-1}$). Different from uniaxial tensile of reinforcements, this test was taken on the periodic boundary condition along three Cartesian directions. The time increment was defined as 0.3 femtoseconds (*fs*). Then an initial velocity with Gaussian distribution was loaded for the structure in

the initialization. We have equilibrated the structure in 500K for 50 *ps* by NPT ensemble. Cooling the system from 500K to 300K within 200 *ps* to make sure it fully relaxed in three Cartesian directions. Later the system was equilibrated again in 300K by NPT ensemble for 50 *ps* to make the structure more stable at the initial state. Then the tensile was taken to the structure in NVT ensemble under a controlling of target temperature 300K. During the tensile in NVT ensemble, the cubic structure is uniformly expanded along with the tensile orientation by stretching the double side in the X orientation. The virial stress was averaged 1 time per picosecond to print the engineering stress-strain response.

After the mechanical properties of reinforcement and matrix were fully explored by uniaxial tensile, an investigation of GN/P3HT and carbon-nitride (C_xN_y)/P3HT nanocomposites was carried out to check the enhancement of the reinforced composite. Here, several structures with Graphene and C_xN_y were packaged as reinforcement inside the P3HT matrix (Fig.2(b)). In this study, a rectangular nanosheet was constructed with a size of width 40.0±2.0 Å, height 20.0±2.0 Å to keep the integrity of the lattice and the adaptability among different GN and C_xN_y nanosheets. Since the integrity of the lattice influences the mechanical response rather than size (see Appendix.C). Those reinforcements were randomly distributed into the matrix. In this study, 5%, 10%, and 15% volume fractions of reinforcement were packaged into a cell size 60.9x60.9x60.9 Å (XxYxZ) with a predefined density of 1.1 g/cm³ for each nanocomposite (Fig.3). The objective of this procedure is to do a comparison for each structure with 5%, 10%, and 15% reinforcement volume fractions. Then compare stress-strain response for each model with different reinforcements by classic Molecular Dynamics (MD) simulation. During the uniaxial test of the nanocomposite, the periodic boundary conditions were carried out to avoid the free-atoms effect on edges of three Cartesian orientations. A *kspace* style with *Ewald* was defined as 1.0e-4 kcal/mol in the GN/P3HT, C_xN_y/P3HT nanocomposite uniaxial tensile; the simulation time increment was chosen with 0.3 *fs*. Pair style and bond style were formulated by the second generation force field named class2 [55]. Then the amorphous structure equilibrated in 500K with the controls of NPT ensemble for 50 *ps*. Later, the system was cooled down from 500K to 300K for 50 *ps* in NPT ensemble. Then we equilibrated the system in 300K by NPT for 50 *ps* to make the structure fully relaxed. Finally, a constant tensile rate of $6.0 \times 10^9 s^{-1}$ was used to elongate the structure in X-direction within the controls of the NVT ensemble at 300K.


(a) 5% Graphene 95% P3HT

(b) 10% Graphene 90% P3HT

(c) 15% Graphene 85% P3HT

(d) 5% C_6N_6 95% P3HT

(e) 10% C_6N_6 90% P3HT

(f) 15% C_6N_6 85% P3HT

Next, a cohesive model was proposed here to explore the interfacial strength between nanosheets (GN, carbon-nitride) and P3HT. In this section, a non-equilibrium molecular dynamics (NEMD) simulation was used to investigate the interfacial strength between carbon-nitride nanosheet and the P3HT bond force of predicted interfacial mechanical properties. In Fig.4, a velocity with 1.0 Å/ps was loaded in the top sheet and the bottom side was fixed in three Cartesian directions. The simulation was taken in non-periodic boundary conditions along the Z-direction since the top carbon-nitride sheet was defined to be separated to 10 nm during the test. And the bottom side which bellows from 20 Å in the orientation of Z was fixed. Here a hybrid potential was used to describe the interaction between sheet materials and matrix. For GN and C$_x$N$_y$ nanosheet, the bond interaction is described by *tersoff* potential. Moreover, the non-bonded interaction between reinforcement (GN, C$_x$N$_y$,) and P3HT has been formulated in van der Waals (vdW) formulation (formula (2)) [55].

$$V(r_{ij}) = \epsilon_{ij}\left[2\left(\frac{\sigma_{ij}}{r_{ij}}\right)^9 - 3\left(\frac{\sigma_{ij}}{r_{ij}}\right)^6\right] \qquad (2)$$

Where ϵ_{ij} represents equilibrium depth, σ_{ij} represents the distance between two atoms promoted by *i* and *j* without bond connection, r_{ij} describes the current distance. However, a covalent bond for the interface between polymer and fillers will not be considered in this study, since the interface break bond potential is not available. In Fig.4, a cubic cell indicates the basic structure of C$_3$N$_4$/P3HT composite with 23806 atoms and 60.2x60.2x65.9 Å length. The structure is topologically optimized and dynamically equilibrated following the same procedures as mentioned above. Fig.13 illustrates the traction evolutions of the normal interface separation. The nanosheet is normally separated. The middle part (from 20 to 60 Å in Z orientation) and other parts are in 300K with NVT ensemble. The system temperature and pressure are controlled by employing the NVT and NPT ensemble, respectively. Other steps are the same as the previous setting in section 2.
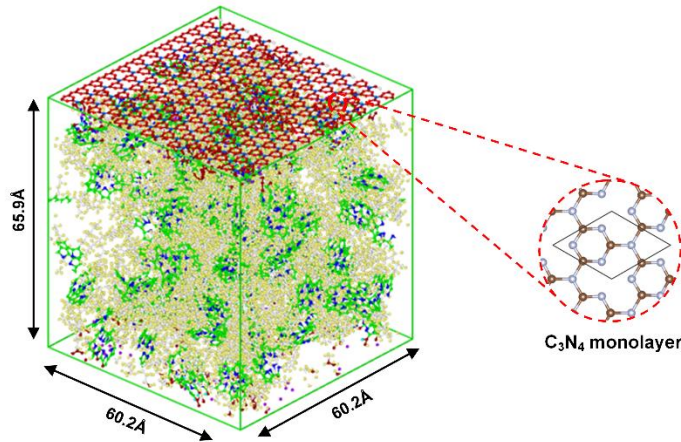
Fig.4, A cubic cell size 60.2x60.2x65.9 Å^3 with a single nanosheet on the top to examine the interface mechanical properties. The depicted composite belongs to C$_3$N$_4$/P3HT with 23806 individual atoms.

3. Results and discussion

We first explore the mechanical properties of the target nanosheets by performing fundamental uniaxial tensile results. The schematic view of stress-strain response to linear relation is shown in Fig.5; followed by a nonlinear response up to the maximum tensile strength, where the maximum load-bearing of the sheet is reached. By further increasing the deformation after the maximum strength point, the stress decreases dramatically, indicating that the damage occurred in the specimen due to the fracture of the bond. This rupture propagation can be found in Fig.8. To evaluate the monolayer anisotropy properties, a uniaxial tensile test was performed along two perpendicular planar orientations called armchair and zigzag, see Fig.2(a). The predicted stress-strain response of graphene and carbon-nitride nanomembranes is compared in Fig.6. It is similar to the mechanical response of the conventional nanomembrane that the slope of the stress-strain curve within linear response represents the elastic modulus. It is

evident from Fig.6 that graphene and other carbon nitride monolayers exhibit an anisotropic strength as depicted stress-strain curve. The armchair tensile strength of GN, C_2N, C_3N, C_3N_4, C_6N_6, and C_7N_6 can be evaluated at 110.60, 66.88, 117.50, 46.78, 44.03, 57.78 GPa, respectively. Compared with armchair direction, zigzag strengths were estimated to be 119.31, 91.97, 119.94, 48.13, 68.84, 62.22 GPa, respectively (Table.1). It is worth mentioning that the stress-strain curves calculated by the classic MD at 300K show a non-physical deformation hardening at a high strain response. A similar response was also found by using AIREBO and REBO potentials as outlined in [60]. To address the non-physical strain hardening issue, the conventional way is to modify the cutoff for the potential. Such work was investigated by AIREBO potential by defining a 2.0 Å [61]. However, the calculated result of the modified cutoff potential with AIREBO potential is not consistent with the finds from the experiment. Therefore, we chose the same method, but a more precise *Tersoff* potential file with the aforementioned cutoff distance to 2.0 and 2.1 Å [62]. It should be mentioned that the thickness of monolayers is not negligible. The thickness of GN and carbon-nitride are 3,35 Å [60], 3,20 Å [30], respectively. So the maximum tensile strength of GN along zigzag can be evaluated as 119.31 GPa (39.97 GPa.nm) which is very close to the previous experiment from Lee et al (130±10 GPa) [27]. The armchair loading direction shows that the maximum tensile strength was evaluated at 110.60 GPa (37.05 GPa.nm) which makes very well agreement with the DFT result at 110 GPa [62].

As expected, the monolayers have an elastic module property since many porosities are made up of GN and C_xN_y structures. To in-depth understand the mechanical property, the armchair elastic modulus of GN, C_2N, C_3N, C_3N_4, C_6N_6, to C_7N_6 were estimated at 100K with 1009.41, 357.03, 1000.24, 559.32, 341.06, and 295.50 GPa, respectively by linear fitting with Origin75 [63] within a linear response of 0.01. In C_7N_6 nanosheet, due to the existence of nanoporosity in the lattice and irregular and non-hexagonal bonding configurations, after equilibration at 300K the structure shows considerable out-of-plane deflection and wrinkling. In this monolayer, at the initial stages of the loading by applying the strain, first the wrinkling suppresses and the sheet becomes more flat, resulting in a smooth increase of the stress. Such that only by further increase of the strain levels starts the bond elongation to evolve resulting in the linear increase of the stress values (see Fig.5 (f)). Therefore, we strongly believe the modulus should be fitted around 0.05. In addition to the evaluation of monolayer anisotropy, material tensile strength with different strain rates was performed to explore the maximum strength that plays a critical role in material prediction. The assessment of maximum stress with different strain rates defines the extensibility of the material's ability to bear loads before fracture. In Fig.5, the maximum strength increases as the strain rates increase. Except for Graphene, C_3N achieved the highest maximum tensile strength with 119.63 GPa (38.28 GPa.nm) across several carbon nitride materials. In this contribution, we confirmed that the stress response of C_3N along the zigzag direction is almost close to the defect-free graphene [40]. Our consequence is only 4.3% different from the reported strength of 36.70 GPa.nm by Liu et al [64]. The overestimated strength can be attributed to the significant large time increment in the loading state. In terms of reinforcement, C_3N exhibits excellent mechanical properties in both armchair and zigzag orientation among several two-dimensional carbon-nitride materials and various reinforcement applications. It can be observed from Fig.5 (d) that the yielding part of C_3N_4 is much more sensitive for the strain rate, and C_6N_6 exhibits also a slightly like C_3N_4 for the mechanical response. This stress fluctuation is around the strain of 0.1. Such a mechanical response is not predictable as the case of the monolayer in C_2N (Fig.5 (b)) or C_3N (Fig.5 (c)) of the other exactly fitted stress-strain curve in the yield zone. By strain state around 0.09, a few nitride atoms will distribute in the normal direction due to C-N debonding. This reduces the bond strength, leads to stress fluctuating in the yield zone. This is why the stress distribution in Fig.7 (d) and (e) is not unified around the crack edge like Fig.7 (a) and (c). Interestingly, the C_7N_6 stress-strain curve shows a remarkably ultrahigh linear response curve as the strain reaching the debonding point of 0.15. This indicates that C_7N_6 has the potential to be a sensor to explore the stress response since it has not only a good linear stress-strain response within a specific domain (strain 0.05-0.15) but also isotropic elasticity, which means that the elastic modulus along armchair and zigzag is the same.
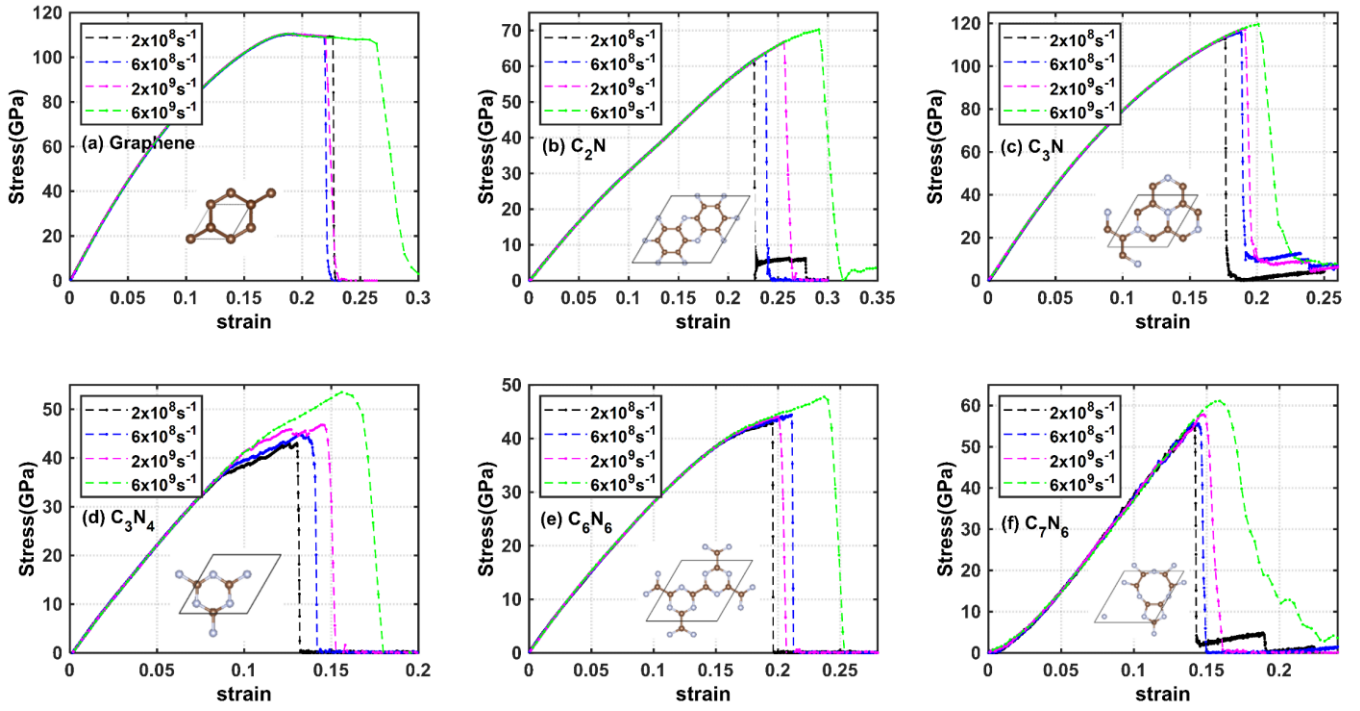
Fig.5, Uniaxial stress-strain relations of different nanosheets elongated at 300K along armchair directions with different strain rates ($2.0 \times 10^8 s^{-1}$, $6.0 \times 10^8 s^{-1}$, $2.0 \times 10^9 s^{-1}$, and $6.0 \times 10^9 s^{-1}$). Inserts depict the single lattice structure of the studied monolayers.

By further investigation, C_2N exhibits the biggest strength difference along with armchair and zigzag, in which the ultimate strength difference reaches 25.09 GPa for C_2N (Table.2). C_2N and C_6N_6 monolayers exhibit an obvious anisotropic strength which can be attributed to strong strain hardening in zigzag orientation after the yield zone. Hereby, the maximum strength along the armchair and zigzag is larger compared with other monolayers at the same boundary condition (see Fig.6). These findings indicate that the mechanical response of C_2N and C_6N_6 is much more sensitive to the load value and orientation.
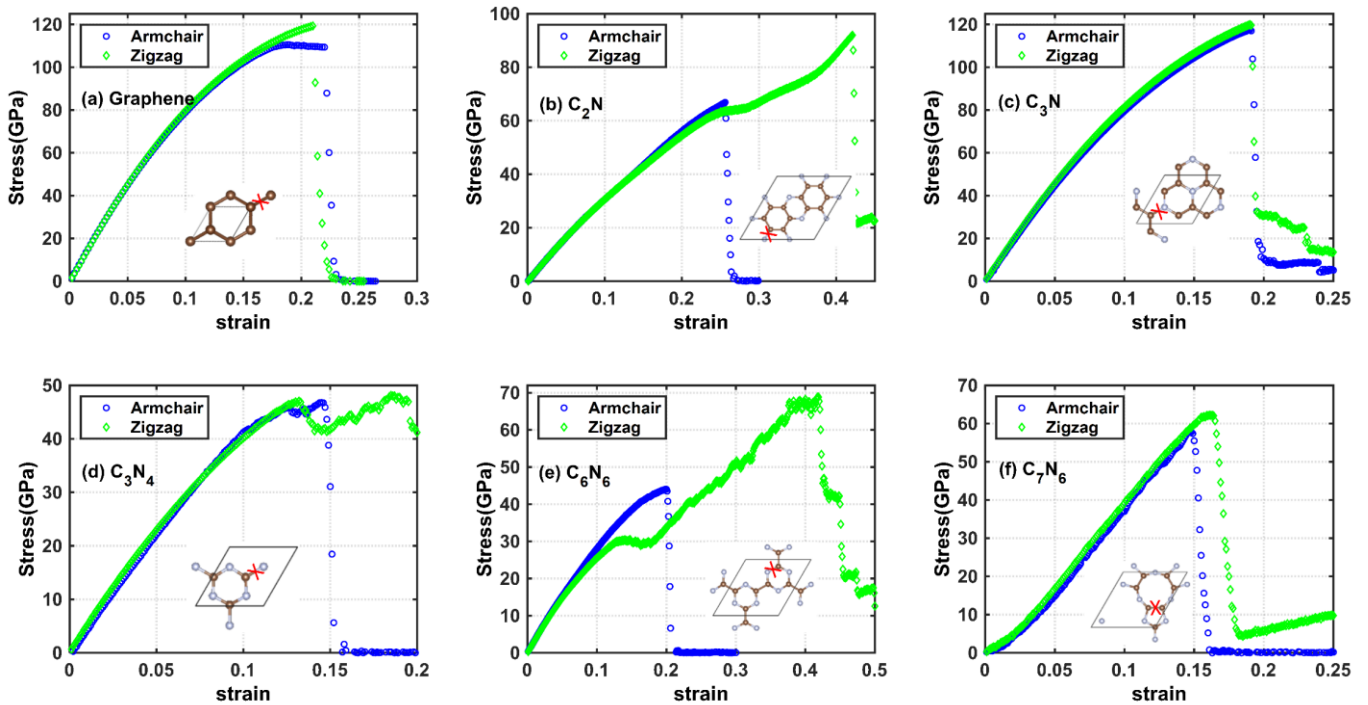
Fig.6, Stress-strain response of different nanosheets elongated along with the armchair and zigzag directions at 300 K with a constant strain rate $2.0 \times 10^9 s^{-1}$. Insets show the atomic lattices and red crosses represent the place at which the first failure occurs for the loading along the armchair direction.

Structure	$\delta=2.0\times10^8 s^{-1}$	$\delta=6.0\times10^8 s^{-1}$	$\delta=2.0\times10^9 s^{-1}$	$\delta=6.0\times10^9 s^{-1}$
C_2N	61.66	63.75	66.88	70.25
C_3N	113.22	115.94	117.50	119.63
C_3N_4	43.03	45.00	46.78	53.50
C_6N_6	43.13	44.44	44.03	47.78
C_7N_6	55.31	55.69	57.78	61.09
Graphene	110.48	110.57	110.60	110.51

Table.1, Maximum tensile strength comparing for graphene and C_xN_y under different loading strain rates (δ) elongated along the armchair at 300 K, units are in GPa.

Structure	$\sigma_{Armchair}$	$\varepsilon_{Armchair}$	σ_{Zigzag}	ε_{Zigzag}
C_2N	66.88	0.26	91.97	0.42
C_3N	117.50	0.19	119.94	0.19
C_3N_4	46.78	0.14	48.13	0.18
C_6N_6	44.03	0.20	68.84	0.42
C_7N_6	57.78	0.15	62.22	0.16
Graphene	110.60	0.19	119.31	0.21

Table.2, Comparison of tensile strength of nanosheets along the armchair and zigzag directions at 300 K with a strain rate of $2.0\times10^9 s^{-1}$, units are in GPa.
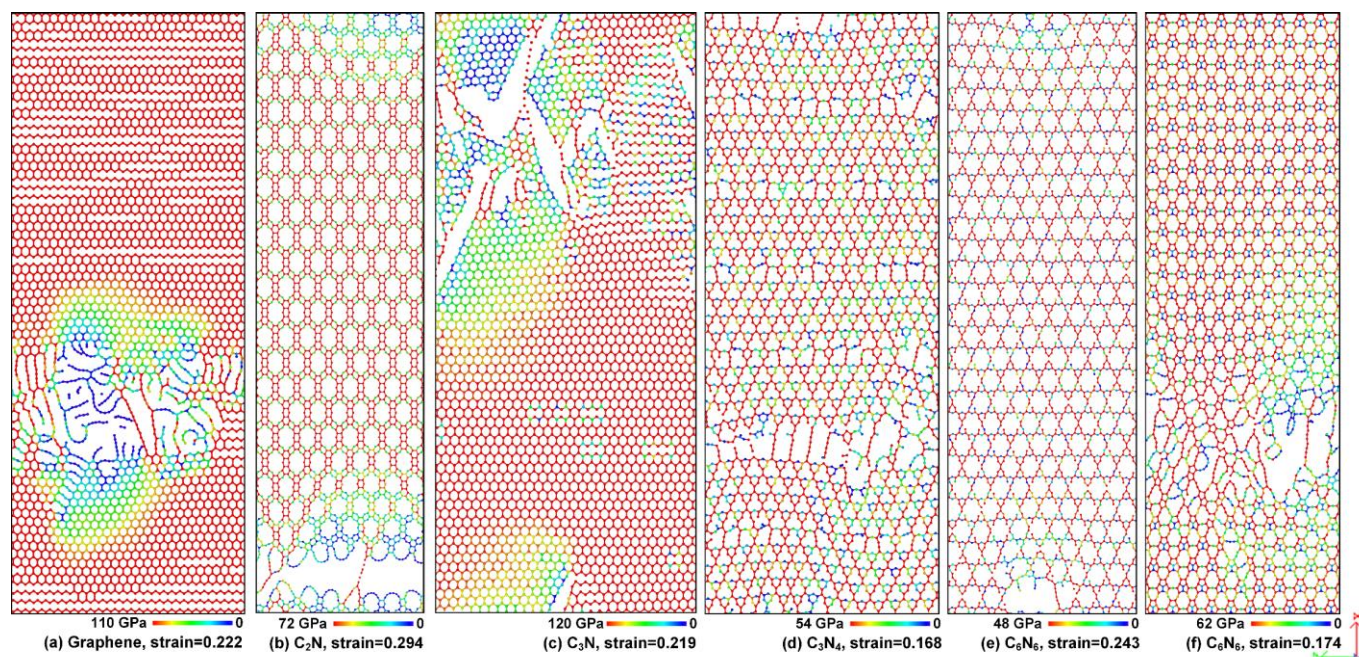
Failure analysis plays an important role in mechanical properties investigation. The strain at the failure point predicts the allowed material stretch before crack initiation in the lattice, which is also an important parameter for the new materials exploration and designing [40]. During the deformation, the bond and the structure are elongated along with the load orientation, which contributes directly to the maintenance and transfer of the load for the structure.

In this section, the focus is put on the crack propagation analysis as well as the debonding analysis during deformation. The 2D nanosheet stress distribution is shown in Fig.7. The crack of the C_2N monolayer appears first at the C-N bond at the strain of 0.294 in Fig.7 (b). The result of the homogeneous stress distribution demonstrates that the C_2N is very stable before the initial crack occurring. In this regard, it is important to achieve a stable material response as the instability leads to material failure at low stress [40]. Moreover, the crack takes place around the top and bottom edge in Fig.7 (c). As the crack tip is blunt, σ_{xx} is almost zero as the surface is traction-free. The brittle failure of C_3N grows in a straight crack path rather than a crooked pattern by the propagation of a sharp crack at a strain of 0.204 in Fig.8(b). This demonstrates a higher brittleness fracture with the comparison of other C_xN_y nanosheets. Comparing with atomic metal materials, whether a porosity 2D material (e.g.C_3N) exhibits a brittle or ductile fracture is related much to the bond strength and the intensity of the atom rather than a porosity for nanoscale cavitation in the region ahead of the crack tip [65]. From Fig.8 (c) to Fig.8 (d), the crack is located on the side of the edge close to the load area. One can observe from the fracture evolution of C_3N in Fig.8 that the rupture of carbon-nitride nanosheets does not appear at the maximum strength immediately (ε=0.190). Instead, the initial fracture occurs at the strain of 0.204 (Fig.8 (b)). It demonstrates that the brittle failure around the crack tip through extensive bonds stretching within a short strain domain, indicative of tiny ductile deformation for C_3N monolayer. One should notice that this tiny ductile deformation is not because of the dissipated energy inside the shear band which could give rise to localized melting [65]. Such rapid crack propagation can be attributed to the C_3N monolayer strain energy release rate exceeds the crack surface energy release rate. Moreover, the fracture occurs initially on the edge and extends to the middle field. It can be confirmed as the previous work [40] that the fracture will take place much more possible around the edge for the fundamental plane stress case. Since the generalized stress intensity defector (GSIF) around the edge is larger than the internal for the same initial crack. Additionally, it is observed that the first debonding of C_7N_6 is the C-C bond. In contrast, the first debonded part of C_2N, C_3N, C_3N_4, C_6N_6 are C-N bonds, which were confirmed from previous DFT work for C_3N_4 [66], C_3N [40]. In other words, those C-N and C-C bonds

limit not only the maximum tensile strength of C_2N, C_3N, C_3N_4, C_6N_6, and C_7N_6, respectively but also influence the analogous deformation. Furthermore, as depicted in Fig.5, the linear elastic response of carbon-nitride nanoporous

| 110 GPa ▬▬ 0 | 72 GPa ▬▬ 0 | 120 GPa ▬▬ 0 | 54 GPa ▬▬ 0 | 48 GPa ▬▬ 0 | 62 GPa ▬▬ 0 |
| (a) Graphene, strain=0.222 | (b) C_2N, strain=0.294 | (c) C_3N, strain=0.219 | (d) C_3N_4, strain=0.168 | (e) C_6N_6, strain=0.243 | (f) C_6N_6, strain=0.174 |

Fig.7, Schematic illustration of the tensile stress (σ_{xx}) distribution for six different monolayers deformed at a constant strain rate of $6.0 \times 10^9 s^{-1}$ at 300K.

(a) strain=0   (b) strain=0.204   (c) strain=0.207   (d) strain=0.225   (e) C_3N overview
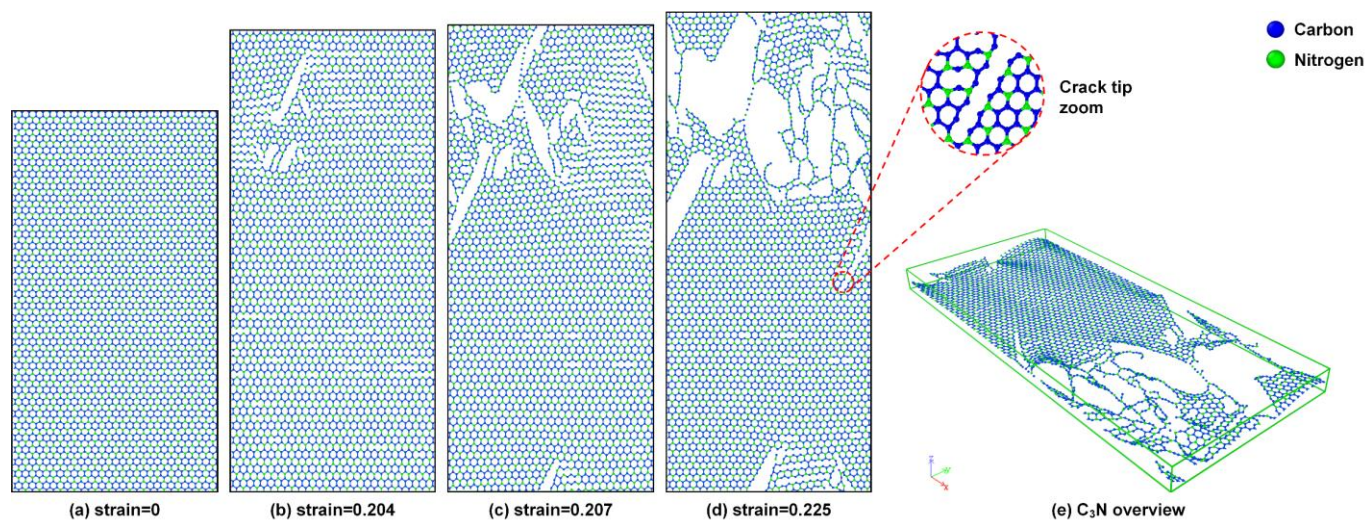
Fig.8, Schematic illustration of C_3N nanosheet deformation during the uniaxial tensile along an armchair direction at 300 K with the constant strain rate of $6.0 \times 10^9 s^{-1}$. The right side is an overview of the C_3N nanosheet at a tensile strain of 0.225.

behaves likely to the defect-free and densely constructed two-dimensional materials, where the deformation of the nanosheet was formed mainly depends on the bond elongation. This can be demonstrated in Fig.7 and Fig.8. Moreover, it is noticed that the deformation was driven mostly by C-C bond elongation at the initial stretching of the monolayer rather than structure deflection. Having this structure deflection at hand can result in higher stretchability than pristine nanosheets [67].

After elaborately analyzing the mechanical properties of nanosheets, we now study the polymer's mechanical response. To validate our P3HT model, the model characterization study was performed by evaluating the P3HT density and elastic modulus. The predicted P3HT density of 1.025 *g/cm³* (ρ_{exp}=1.1 *g/cm³* [68,69]) at the heating rate of 5.56 *K/ps*. The slight density discrepancy could be attributed to the short equilibrium time domain at 300K. It should be noticed that the tensile stress was processed with Gaussian SMOOTDATA via MATLAB to reduce the noise from the test data, as depicted in Fig.9 (a). The maximum and minimal peak stress are 122.91, 73.83 MPa at the strain of

0.15 with a constant strain rate of $4.0 \times 10^{10} s^{-1}$, $2.0 \times 10^{9} s^{-1}$, respectively. With the point of the elastic modulus, our calculated tensile modulus is E=1.238 GPa (strain rate $4.0 \times 10^{10} s^{-1}$, 300K), this result confirmed that our MD model is valid with the comparison of previous experiments 1.09 ± 0.15 GPa [70].
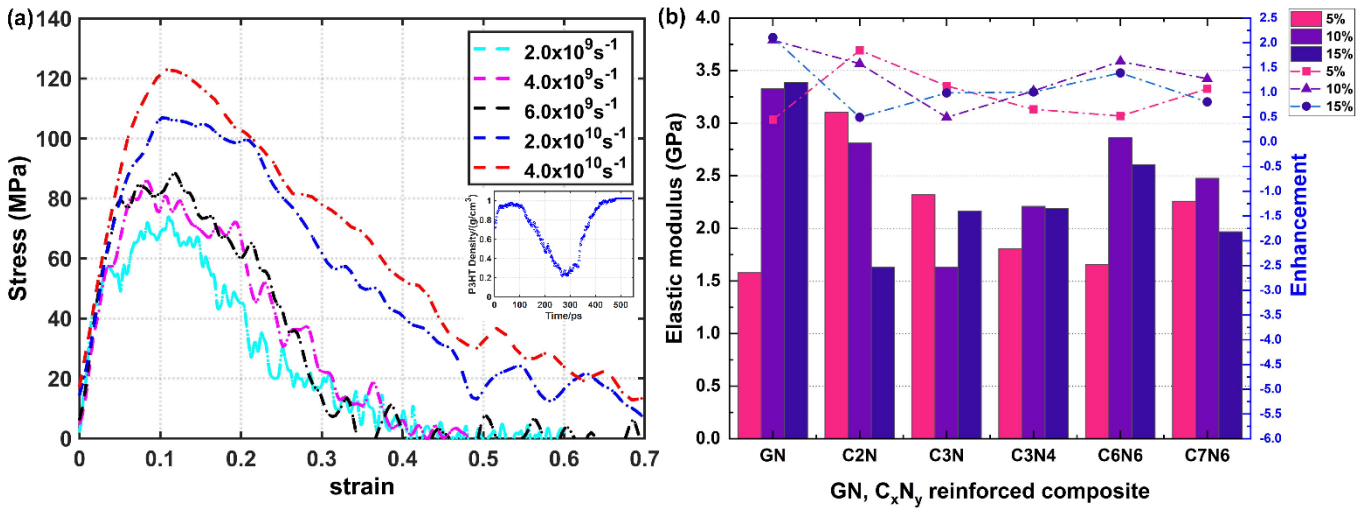

Fig.9, (a) stress-strain relationship of different strain rates comparison for pristine P3HT polymer elongated along X-direction. The inset shows the evolution of density during the heating and cooling rate of 5.56K/ps; (b) the elastic modulus and the enhancements of the GN, C_xN_y/P3HT composites with the volume fraction from 5% to 15% at 300K, compared to pristine P3HT.

Next, the maximum strength of the reinforced nanocomposites for various volume fractions during the uniaxial tensile and the composite elastic modulus is presented in Fig.9 (b) and Fig.10, respectively. From Fig.9 (b), we find out that 15%GN/85% P3HT composite possesses the maximum elastic modulus (3.386 GPa) which can enhance the elastic modulus more than 3 times compared to the pure matrix. Apart from this, 10% GN and 5% C_2N can also enhance the elastic modulus over 3.0 GPa, GN/P3HT modulus get increases as graphene volume fraction increases. However, the C_2N/P3HT elastic modulus presents an opposing, for more detailed the interested reader is referred to Appendix B. The tensile result in Fig.10 reveals that the GN/P3HT nanocomposite has the highest maximum strength among many nanocomposites. The maximum strength can be gotten in 15% GN/85%P3HT composite, σ_{max}=182.65 MPa (ε=0.11). It can be observed from the mechanical response of the C_2N/P3HT composite that such a nanocomposite strength decreases parallel to the filler ratios increasing from 5% to 15% in Fig.10 (b). This phenomenon attributes to the percolation threshold of the composite [16] and the enhancing threshold domain. Since the composite strengthening effect can be valid when the filler ratio reaches such a threshold value and domain that the stiffening mechanism can dominate the objective behavior of the composites. For the same boundary condition, the peak strength from GN/P3HT stress-strain curve exhibits the opposite mechanical response with respect to the within filler ratio of the threshold value (see Fig.10 (a)). Consequently, we conclude that enhancement can be improved only within a certain threshold domain of filler ratio in this study. This ratio could lead to the composite mechanical response difference since nanocomposite tensile strength can increase only in one specific domain (e.g. within 2-5%). When the inclusion ratio exceeds the maximum strengthening threshold, the composite tensile strength might decrease by further increasing of the nanofillers. For higher volume fractions, the mobility of the nanofillers might be restricted by adjacent particles as compared with the sample with a lower ratio of nanofillers [16]. Furthermore, adding more nanofillers may increase the stress concentration and facilitate crack formation and growth. In that case, the higher possibility of the crack formation will play the main role in decreasing the tensile strength rather than the enhanced interaction between reinforcement and matrix. Additionally, there is a filler ratio convergence effect for the carbon-nitride composite mechanical response; in which the peak strength of the composite will not be changed much as the filler volume fraction reaches the mechanical saturation. That is the reason why the maximum strength of the C_7N_6/P3HT is around 140 MPa at different filler ratios. This can be shown significantly in Fig.10 (f) of the strain-strain curve. Next, comparing with a pure P3HT matrix with a strength of 88.34 MPa at a constant strain rate of $6.0 \times 10^{9} s^{-1}$ test, the strength of 10%, 15% Graphene; 5%, 10% C_2N; 10%, 15% C_6N_6; 10% C_7N_6 can reach over 150

MPa, which can enhance the composite's maximum tensile strength to 70 %. Surprisingly, the volume fraction of 15% GN can enhance strength to around 106.76% (Table.3). By observing the deformation behavior, the reinforced nanocomposite stress did not drop dramatically after achieving the peak stress. As the reinforcement was mixed into the P3HT matrix, the traction between reinforcement and polymatrix increases the yield stress by the cavitation or energy dissipation of composite damage. This strengthen can be shown in a mechanical response that the reinforced nanocomposite (15% $C_2N/85\%$P3HT) can be elongated more even though the stress reaches the yield point. Such a volume fraction of C_2N can efficiently overcome the shortage of pristine P3HT with low stretchability. Furthermore, the randomly distributed GN with 10% and 15% exhibit stronger mechanical response with over 170 MPa strength, which can be attributed to the remarkable mechanical properties of GN and strong interface non-bond interaction. The stronger non-bonded interaction contributes to a higher strength density of P3HT at the interface of reinforcement and polymer matrix. For analyzing the non-bond interaction, the normal interface strength will be discussed in the following section.
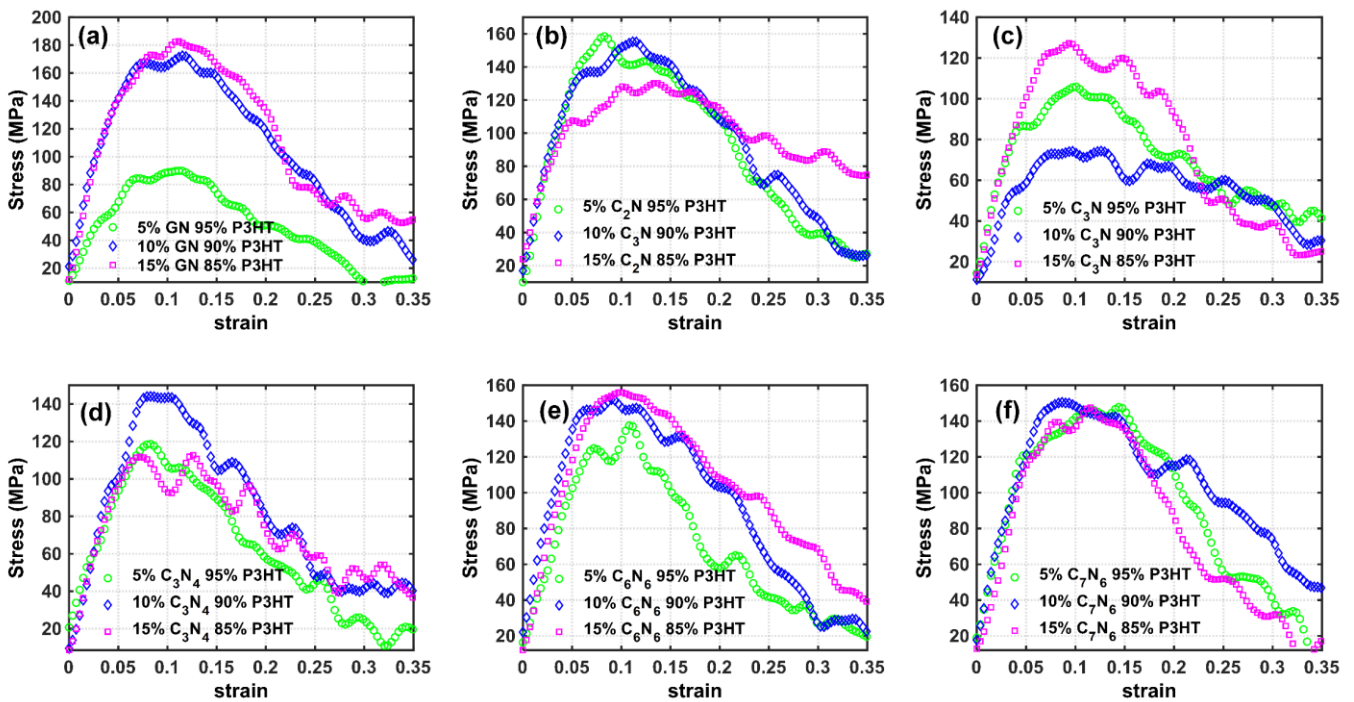
Fig.10, Schematic illustration of stress-strain response of (Graphene, C_xN_y) / P3HT composite with different volume fraction (5%, 10%, 15%) at the constant strain rate of $6.0 \times 10^9 s^{-1}$ at a fixed temperature of 300K.

| Volume fraction	5%C_xN_y 95P3HT	10%C_xN_y 90%P3HT	15%C_xN_y 85%P3HT
C_2N/P3HT	158.51	155.21	130.12
C_3N/P3HT	105.88	74.32	127.23
C_3N_4/P3HT	118.61	144.07	112.68
C_6N_6/P3HT	137.50	152.02	155.99
C_7N_6/P3HT	147.82	150.49	147.50
GN/P3HT	89.94	172.42	182.65

Table.3, Maximum strength of the reinforcement nanocomposite with different volume fractions during the uniaxial tensile, unit (MPa).

After careful examination of the mechanical properties of nanosheets and polymer, we are now prepared to study the effective mechanical properties of nanocomposites. Two typical nanocomposites were selected for failure analysis. In Fig.11, the initial crack occurs when the strain reaches 0.259 at the cubic top and the crack surface was highlighted with a red curve based on the cavitation in the composite. When the strain reaches 0.338, the GN/P3HT crack extends further from the edge to the middle. As the model was elongated further distances, the crack became larger

until the cubic model was completely damaged. Meanwhile, most damage occurs inside the matrix, instead of the interface area. In this study, this result indicates that the interaction of the GN and P3HT has a stronger interaction strength than the strength of the matrix itself. Therefore, the crack occurs in the matrix rather than in the interface zone. This description can be traced back to a contribution from Yuan et al. [71] in his damage test of Graphene/PE composite. Our investigation is also intended for this explanation. Also, during the 15% GN/85% P3HT nanocomposite uniaxial test, the crack appears in the matrix. It should be emphasized that the 15% C_6N_6/85% P3HT composite has a higher capability for fracture resistance. Because the initial crack of 15% C_6N_6/85% P3HT composite appears at the strain of ε=0.295 (Fig.12), compared to the 15% GN/85% P3HT crack strain of 0.259. One should recognize that the fracture mechanism between GN/P3HT and C_6N_6/P3HT has a significant difference. The graphene plays as a barrier in front of the crack growth from the matrix since the filler topology is much bigger than the crack tip and the bond and atoms of GN topology are stable. Such integrity and stability of the GN lattice will keep high mechanical performance for a filler (see Appendix.C). This performance from GN can enhance the mechanical response of the composite during the uniaxial tensile somehow. However, this enhancement can only be regarded as passive mechanical property improvement. In contrast, the filler of C_6N_6/P3HT is almost dissolved in the matrix as well as the bond and atoms are connected together with the numerous atoms of the matrix. This will lead to sufficient interaction between filler and matrix which will also enhance the mechanical property effectively. This sufficient interaction is due to the enhancement network by the percolation of C, N atom from filler rather than the single-phase enhancement mechanism of the filler. Therefore, when damage evolves around the filler, this will resist the crack propagation in an active way which sufficient interaction will play a key role to prevent damage. That is also the reason why did the initial crack of C_6N_6/P3HT appearing at a higher level strain. As the extended distance increases, the crack first appears inside and extends to the edge. It can be concluded that C_6N_6/P3HT nanocomposite is tougher than GN/P3HT composite at the same filler volume fraction concerning the initial crack occurring from Fig.11 to Fig.12.
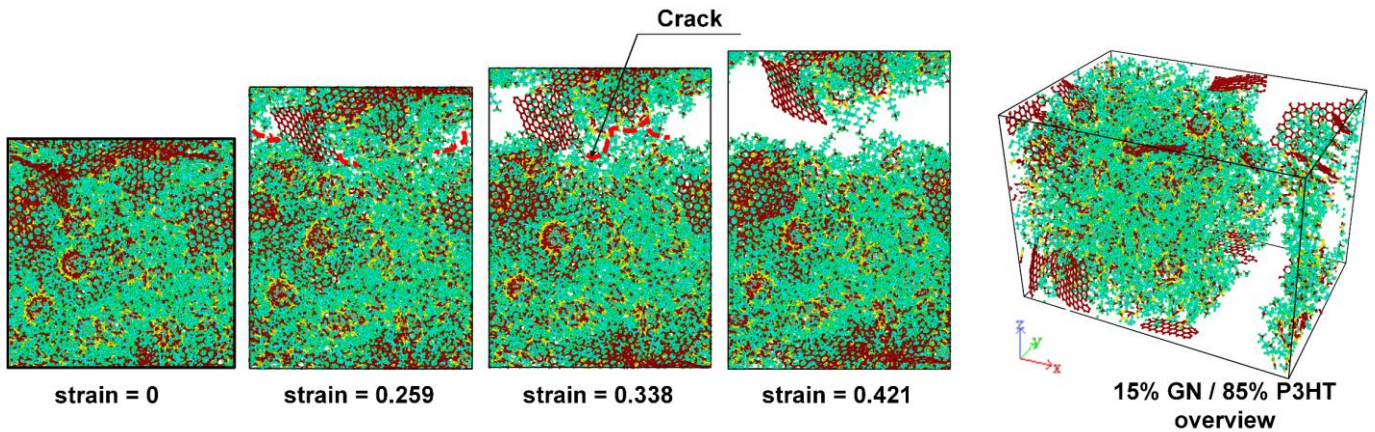
**Fig.11, Mechanical deformation of 15% graphene, 85% P3HT nanocomposite at different strains.**
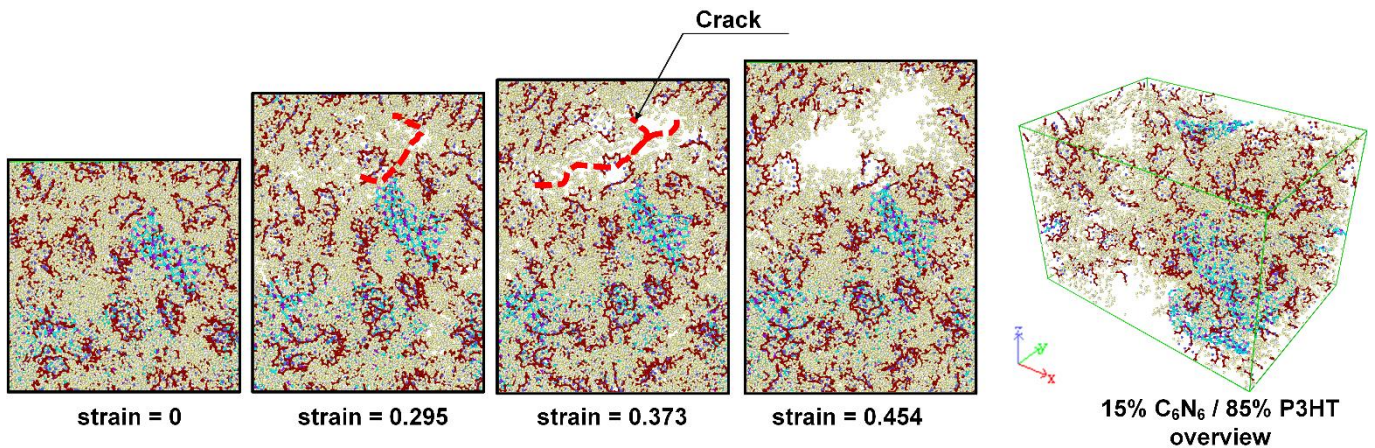
Fig.12, Mechanical deformation of 15% C_6N_6, 85% P3HT nanocomposite at different strains.

The interface strength between reinforcement (GN, C_xN_y) and P3HT polymer influences the not only crack propagation but also the strength of nanocomposites [72]. It has been demonstrated that bond and non-bond

interaction formed inside the polymer play a crucial role in the mechanical properties enhancements [73–75]. In this section, we find out that C_2N/P3HT interface possesses the highest non-bond during interfacial strength comparisons as depicted in Fig.13. The traction separation graph shows that the maximum traction was achieved at 331.94 MPa (0.55 nm). The C_6N_6/P3HT composite has the lowest interfacial strength of 184.24 MPa at the same separating distance. Moreover, the normal traction of GN, C_3N_4, and C_7N_6 is nearly identical with approximately 300 MPa. By observing from Fig.13, the peak traction of the C_2N/P3HT interface is over 1.5 times the lowest (C_6N_6/P3HT). Moreover, all the interfacial strengths are larger than the strength of the pure P3HT matrix (maximum strength 122.91 MPa).
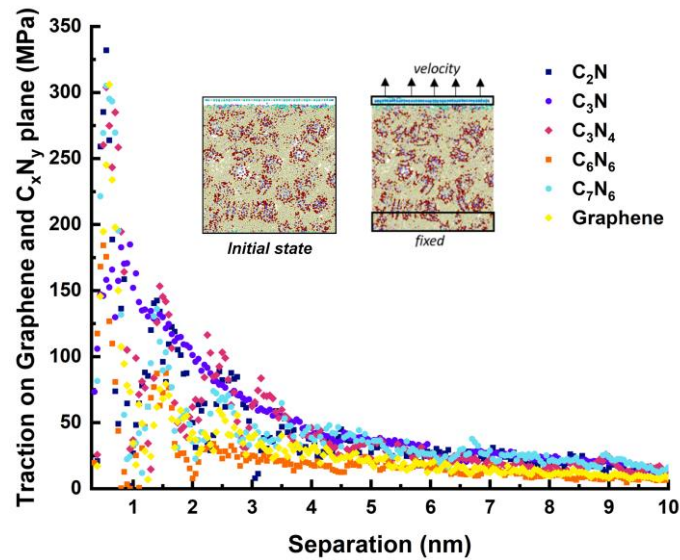
Fig.13, Traction-separation comparing on GN and C_xN_y nanosheet from P3HT polymer matrix with the increase of the separation distance; the internal graphs are the initial and fixing state.

Based on the test, we can conclude that the interfacial strength between the reinforcement (graphene, C_xN_y) and P3HT matrix is larger than the pure P3HT tensile strength. A rupture result from Fig.11 to Fig.12 also reveals that the initial crack takes place in the matrix rather than the interface zone. Because the interfacial non-bond interaction can bear a much bigger load than the matrix. Therefore, a crack will firstly take place in the weakest strength area. Even though stronger traction was constructed in the interface area, the van der Waals (vdW) and Columbic potential depend heavily on the distance between two atoms. Such a distance is the cutoff in which the sheet atoms are beyond the cutoff, the strong interaction will drop dramatically to zero. The higher interface interaction can only function correctly within a valid cutoff for the interaction among the elements of C, H, O, N, etc. The non-bond energy consists of vdW and electrostatic energy which can be formulated as

$$E_{nonbond} = E_{vanderWaals} + E_{electrostatic} \qquad (3)$$

The non-bond interaction potential relies more on vdW, since the electrostatic energy is much lower for a polymer case, as outlined in [42]. Therefore, we believe that the crack will occur in the interface during the separation of the nanosheets from the matrix in our case (our results support these assumptions). Such a perspective of enhancement is understandable from the interface strength for the GN and carbon-nitride composites. It is known that the non-bond interaction between reinforcements and matrix is valid within a cutoff following the van der Waals energy. However, a previous test reported that a crack occurred in the matrix phase instead of the interface region of the graphene/PE separation [76]. This result represents that there is a stronger non-bond interaction between GN and PE interface. It is expected that this interaction will be greater than the covalent bonds of the polymer. However, we observed an alternative response in our results, summarized next. When the crack takes place inside the polymer, the maximum strength will be limited by the polymer's maximum strength. This is due to failure appearance which always takes place at the weakest part of the materials. Therefore, it is difficult to achieve a maximum tensile strength that is higher than the matrix. It should be also noted that there is the possibility of covalent bond formation between nanosheets and polymer, provided that nanofillers are surface functionalized. In the current study we however only consider pristine sheets, without functionalization groups over their surfaces and such that evolution of chemical bonds between nanofillers and polymer are negligible.

For a vacuum interface area, there is no bonded interaction, there should not be any hardening of bonded material. Furthermore, when the separated distance is beyond the cutoff, the non-bond potential is no longer valid, the traction should be almost zero. As a result, it can be observed that the traction drops significantly once the separation reaches 4 nm. Therefore, a crack will appear in the interface zone for the cohesive model. Another work from Zeshuai et al [71] reveals that whether a crack taking place in the matrix or the interface part will depend much on the ratio of the maximum interface strength and matrix strength. The fracture of composite is complicated, non-bond interaction is one of the key criteria for the initial crack appearing. The criterion for the initial crack appearing inside the matrix or the interface needs to be further studied especially for more complicated materials. Our study investigated one of the important factors for the crack appearing and the conclusion fits well in our case. For a more complicated case, more conditions need to be considered during the crack investigation.

3. Conclusions

In this study, we systematically studied the role of graphene and carbon nitride nanosheets in improving the mechanical properties of P3HT polymer by conducting extensive molecular dynamics simulations. We first studied the mechanical/failure responses of carbon-based nanofillers. Graphene as expected yields the highest elastic modulus and tensile strength among the considered nanosheets. Analysis of the mechanical properties of the carbon-nitride sheet reveals that C_3N nanosheet exhibits the highest strength owing to its graphene-like lattice. C_3N_4 monolayer on the other hand yields the lowest tensile strength due to its low-density and porous structure. During the tensile deformation for C_2N, C_3N, C_3N_4, C_6N_6 monolayers, the first debonding occurs C-N bonds. We next elaborately compared the effective mechanical properties of various nanocomposites with different content of nanosheets. Moreover, the traction and separation relations between various nanofillers and polymer matrices were examined to investigate the formed interfacial strength. Our results confirm that the excellent reinforcing performance of graphene and carbon-nitride nanosheet is not only attributed to the outstanding stiffness of these covalent networks but also due to considerable interfacial non-bonding interactions between nanomembranes and polymer matrix. Taking into account that unlike graphene, carbon-nitride nanosheets are mostly intrinsic semiconductors, our findings can be useful to design novel strong semiconducting polymer nanocomposites.

References

[1]   Günes S, Neugebauer H, Sariciftci NS. Conjugated Polymer-Based Organic Solar Cells. Chem Rev 2007;107:1324–38. https://doi.org/10.1021/cr050149z.

[2]   Li G, Zhu R, Yang Y. Polymer solar cells. Nat Photonics 2012;6:153–61. https://doi.org/10.1038/nphoton.2012.11.

[3]   Indah Sari FN, Liu Y-C, Ting J-M. Synthesis of MoS2/MoO3 or P3HT nanocomposites consisting of sandwich-like structures via environmental benign supercritical fluid CO2 and its use in supercapacitor. Compos Part B Eng 2019;177:107355. https://doi.org/10.1016/j.compositesb.2019.107355.

[4]   Wang D, Su Y, Chen D, Wang L, Xiang X, Zhu D. Preparation and characterization of poly(3-octylthiophene)/carbon fiber thermoelectric composite materials. Compos Part B Eng 2015;69:467–71. https://doi.org/10.1016/j.compositesb.2014.10.007.

[5]   Trznadel M, Pron A, Zagorska M, Chrzaszcz R, Pielichowski J. Effect of Molecular Weight on Spectroscopic and Spectroelectrochemical Properties of Regioregular Poly(3-hexylthiophene). Macromolecules 1998;31:5051–8. https://doi.org/10.1021/ma970627a.

[6]   Printz AD, Zaretski A V, Savagatrup S, Chiang ASC, Lipomi DJ. Yield Point of Semiconducting Polymer Films on Stretchable Substrates Determined by Onset of Buckling. ACS Appl Mater Interfaces 2015;7:23257–64. https://doi.org/10.1021/acsami.5b08628.

[7]   Gargi D, Kline RJ, DeLongchamp DM, Fischer DA, Toney MF, O'Connor BT. Charge Transport in Highly Face-On

Poly(3-hexylthiophene) Films. J Phys Chem C 2013;117:17421–8. https://doi.org/10.1021/jp4050644.

[8]   Zhang L, Li Y, Shi J, Shi G, Cao S. Nonvolatile rewritable memory device based on solution-processable graphene/poly(3-hexylthiophene) nanocomposite. Mater Chem Phys 2013;142:626–32. https://doi.org/10.1016/j.matchemphys.2013.08.007.

[9]   Aoyama Y, Douhéret O, Leclère P, Moerman D, Mizukado J, Suda H, et al. On the influence of the photo-oxidation of P3HT on the conductivity of photoactive film of P3HT:PCBM bulk heterojunctions. Org Electron 2017;43:142–7. https://doi.org/10.1016/j.orgel.2017.01.025.

[10]   Liao W-P, Wu J-J. Efficient Electron Collection in Hybrid Polymer Solar Cells: In-Situ-Generated ZnO/Poly(3-hexylthiophene) Scaffolded by a TiO 2 Nanorod Array. J Phys Chem Lett 2013;4:1983–8. https://doi.org/10.1021/jz400996d.

[11]   Thummalakunta LNSA, Yong CH, Ananthanarayanan K, Luther J. P3HT based solution-processed pseudo bi-layer organic solar cell with enhanced performance. Org Electron 2012;13:2008–16. https://doi.org/10.1016/j.orgel.2012.05.054.

[12]   Xu Y, Wang X, Zhou J, Song B, Jiang Z, Lee EMY, et al. Molecular engineered conjugated polymer with high thermal conductivity. Sci Adv 2018;4:eaar3031. https://doi.org/10.1126/sciadv.aar3031.

[13]   Savagatrup S, Printz AD, Rodriquez D, Lipomi DJ. Best of Both Worlds: Conjugated Polymers Exhibiting Good Photovoltaic Behavior and High Tensile Elasticity. Macromolecules 2014;47:1981–92. https://doi.org/10.1021/ma500286d.

[14]   Müller C. On the glass transition of polymer semiconductors and its impact on polymer solar cell stability. Chem Mater 2015;27:2740–54. https://doi.org/10.1021/acs.chemmater.5b00024.

[15]   Rogers JA, Someya T, Huang Y. Materials and Mechanics for Stretchable Electronics. Science (80-) 2010;327:1603–7. https://doi.org/10.1126/science.1182383.

[16]   Gersappe D. Molecular Mechanisms of Failure in Polymer Nanocomposites. Phys Rev Lett 2002;89:058301. https://doi.org/10.1103/PhysRevLett.89.058301.

[17]   Hatam-Lee SM, Rajabpour A, Volz S. Thermal conductivity of graphene polymorphs and compounds: From C3N to graphdiyne lattices. Carbon N Y 2020;161:816–26. https://doi.org/10.1016/j.carbon.2020.02.007.

[18]   Zhang Q, Mortazavi B, Aldakheel F. Molecular Dynamics Modeling of Mechanical Properties of Polymer Nanocomposites Reinforced by C7N6 Nanosheet. Surfaces 2021;4:240–54. https://doi.org/10.3390/surfaces4030019.

[19]   Hatam-Lee SM, Rajabpour A, Volz S. Thermal conductivity of graphene polymorphs and compounds: From C3N to graphdiyne lattices. Carbon N Y 2020;161:816–26. https://doi.org/10.1016/j.carbon.2020.02.007.

[20]   Kiani L, Hasanzadeh J, Yousefi F, Anaraki PA. Phonon modes contribution in thermal rectification in graphene-C3B junction: A molecular dynamics study. Phys E Low-Dimensional Syst Nanostructures 2021;131:114724. https://doi.org/10.1016/j.physe.2021.114724.

[21]   Fooladpanjeh S, Yousefi F, Molaei F, Zarghami Dehaghani M, Sajadi SM, Abida O, et al. Thermal conductivity of random polycrystalline BC3 nanosheets: A step towards realistic simulation of 2D structures. J Mol Graph Model 2021;107:107977. https://doi.org/10.1016/J.JMGM.2021.107977.

[22]   Razzaghi L, Khoeini F, Rajabpour A, Khalkhali M. Thermal transport in two-dimensional C3N/C2N superlattices: A molecular dynamics approach. Int J Heat Mass Transf 2021;177:121561. https://doi.org/10.1016/J.IJHEATMASSTRANSFER.2021.121561.

[23]   Arabha S, Rajabpour A. Thermo-mechanical properties of nitrogenated holey graphene (C2N): A comparison of machine-learning-based and classical interatomic potentials. Int J Heat Mass Transf 2021;178:121589. https://doi.org/10.1016/j.ijheatmasstransfer.2021.121589.

[24]   Farzadian O, Yousefi F, Spitas C, Kostas KV. Phonon heat transport in two-dimensional phagraphene-graphene superlattice. Int J Heat Mass Transf 2022;182:121917. https://doi.org/10.1016/J.IJHEATMASSTRANSFER.2021.121917.

[25]   Castro Neto AH, Guinea F, Peres NMR, Novoselov KS, Geim AK. The electronic properties of graphene. Rev Mod Phys 2009;81:109–62. https://doi.org/10.1103/RevModPhys.81.109.

[26]   Shahil KMF, Balandin AA. Graphene–Multilayer Graphene Nanocomposites as Highly Efficient Thermal Interface Materials. Nano Lett 2012;12:861–7. https://doi.org/10.1021/nl203906r.

[27]   Lee C, Wei X, Kysar JW, Hone J. Measurement of the Elastic Properties and Intrinsic Strength of Monolayer Graphene.

1   Science (80-) 2008;321:385–8. https://doi.org/10.1126/science.1157996.

2   [28]   Guo Z, Song L, Boay CG, Li Z, Li Y, Wang Z. A new multiscale numerical characterization of mechanical properties of

3   graphene-reinforced polymer-matrix composites. Compos Struct 2018;199:1–9.

4   https://doi.org/10.1016/j.compstruct.2018.05.053.

5   [29]   Raccichini R, Varzi A, Passerini S, Scrosati B. The role of graphene for electrochemical energy storage. Nat Mater

6   2015. https://doi.org/10.1038/nmat4170.

7   [30]   Xu Y, Wang X, Zhou J, Song B, Jiang Z, Lee EMY, et al. Molecular engineered conjugated polymer with high thermal

8   conductivity. Sci Adv 2018;4:1–7. https://doi.org/10.1126/sciadv.aar3031.

9   [31]   Cho E-C, Huang J-H, Li C-P, Chang-Jian C-W, Lee K-C, Hsiao Y-S, et al. Graphene-based thermoplastic composites

10   and their application for LED thermal management. Carbon N Y 2016;102:66–73.

11   https://doi.org/10.1016/j.carbon.2016.01.097.

12   [32]   Shtein M, Nadiv R, Buzaglo M, Regev O. Graphene-Based Hybrid Composites for Efficient Thermal Management of

13   Electronic Devices. ACS Appl Mater Interfaces 2015. https://doi.org/10.1021/acsami.5b07866.

14   [33]   Liu L, Niu Z, Zhang L, Zhou W, Chen X, Xie S. Nanostructured graphene composite papers for highly flexible and

15   foldable supercapacitors. Adv Mater 2014. https://doi.org/10.1002/adma.201401513.

16   [34]   Yang J, Qi GQ, Liu Y, Bao RY, Liu ZY, Yang W, et al. Hybrid graphene aerogels/phase change material composites:

17   Thermal conductivity, shape-stabilization and light-to-thermal energy storage. Carbon N Y 2016.

18   https://doi.org/10.1016/j.carbon.2016.01.063.

19   [35]   Bae SH, Lee Y, Sharma BK, Lee HJ, Kim JH, Ahn JH. Graphene-based transparent strain sensor. Carbon N Y 2013.

20   https://doi.org/10.1016/j.carbon.2012.08.048.

21   [36]   Lou Z, Chen S, Wang L, Jiang K, Shen G. An ultra-sensitive and rapid response speed graphene pressure sensors for

22   electronic skin and health monitoring. Nano Energy 2016;23:7–14. https://doi.org/10.1016/j.nanoen.2016.02.053.

23   [37]   Rafiee MA, Rafiee J, Wang Z, Song H, Yu ZZ, Koratkar N. Enhanced mechanical properties of nanocomposites at low

24   graphene content. ACS Nano 2009. https://doi.org/10.1021/nn9010472.

25   [38]   Li Y, Wang Q, Wang S. A review on enhancement of mechanical and tribological properties of polymer composites

26   reinforced by carbon nanotubes and graphene sheet: Molecular dynamics simulations. Compos Part B Eng

27   2019;160:348–61. https://doi.org/10.1016/j.compositesb.2018.12.026.

28   [39]   Stankovich S, Dikin DA, Dommett GHB, Kohlhaas KM, Zimney EJ, Stach EA, et al. Graphene-based composite

29   materials. Nature 2006. https://doi.org/10.1038/nature04969.

30   [40]   Mortazavi B. Ultra high stiffness and thermal conductivity of graphene like C3N. Carbon N Y 2017;118:25–34.

31   https://doi.org/10.1016/j.carbon.2017.03.029.

32   [41]   Yang S, Li W, Ye C, Wang G, Tian H, Zhu C, et al. C3N—A 2D Crystalline, Hole-Free, Tunable-Narrow-Bandgap

33   Semiconductor with Ferromagnetic Properties. Adv Mater 2017. https://doi.org/10.1002/adma.201605625.

34   [42]   Ji WM, Zhang LW, Liew KM. Understanding interfacial interaction characteristics of carbon nitride reinforced epoxy

35   composites from atomistic insights. Carbon N Y 2021;171:45–54. https://doi.org/10.1016/j.carbon.2020.08.067.

36   [43]   Kumar P, Vahidzadeh E, Thakur UK, Kar P, Alam KM, Goswami A, et al. C 3 N 5 : A Low Bandgap Semiconductor

37   Containing an Azo-Linked Carbon Nitride Framework for Photocatalytic, Photovoltaic and Adsorbent Applications. J Am

38   Chem Soc 2019;141:5415–36. https://doi.org/10.1021/jacs.9b00144.

39   [44]   Tiwari S, Singh AK, Prakash R. Poly(3-hexylthiophene) (P3HT)/Graphene nanocomposite material based organic field

40   effect transistor with enhanced mobility. J Nanosci Nanotechnol 2014;14:2823–8. https://doi.org/10.1166/jnn.2014.8570.

41   [45]   Sun H. Compass: An ab initio force-field optimized for condensed-phase applications - Overview with details on alkane

42   and benzene compounds. J Phys Chem B 1998. https://doi.org/10.1021/jp980939v.

43   [46]   Shiu SC, Tsai JL. Characterizing thermal and mechanical properties of graphene/epoxy nanocomposites. Compos Part

44   B Eng 2014. https://doi.org/10.1016/j.compositesb.2013.09.007.

45   [47]   Momma K, Izumi F. VESTA 3 for three-dimensional visualization of crystal, volumetric and morphology data. J Appl

46   Crystallogr 2011;44:1272–6. https://doi.org/10.1107/S0021889811038970.

47   [48]   Stukowski A. Visualization and analysis of atomistic simulation data with OVITO–the Open Visualization Tool. Model

48   Simul Mater Sci Eng 2010;18:015012. https://doi.org/10.1088/0965-0393/18/1/015012.

49   [49]   Tersoff J. Empirical interatomic potential for carbon, with applications to amorphous carbon. Phys Rev Lett

50   1988;61:2879–82. https://doi.org/10.1103/PhysRevLett.61.2879.

[50] Tersoff J. New empirical approach for the structure and energy of covalent systems. Phys Rev B 1988;37:6991–7000. https://doi.org/10.1103/PhysRevB.37.6991.

[51] Lindsay L, Broido DA. Optimized Tersoff and Brenner empirical potential parameters for lattice dynamics and phonon thermal transport in carbon nanotubes and graphene. Phys Rev B - Condens Matter Mater Phys 2010;81:1–6. https://doi.org/10.1103/PhysRevB.81.205441.

[52] KInacI A, Haskins JB, Sevik C, ÇağIn T. Thermal conductivity of BN-C nanostructures. Phys Rev B - Condens Matter Mater Phys 2012. https://doi.org/10.1103/PhysRevB.86.115410.

[53] Lipomi DJ, Tee BCK, Vosgueritchian M, Bao Z. Stretchable organic solar cells. Adv Mater 2011. https://doi.org/10.1002/adma.201004426.

[54] Mortazavi B, Fan Z, Pereira LFC, Harju A, Rabczuk T. Amorphized graphene: A stiff material with low thermal conductivity. Carbon N Y 2016;103:318–26. https://doi.org/10.1016/j.carbon.2016.03.007.

[55] Sharma S. Molecular Dynamics Simulation of Nanocomposites Using BIOVIA Materials Studio, Lammps and Gromacs. Elsevier; 2019. https://doi.org/10.1016/C2017-0-04396-3.

[56] Plimpton S. Fast Parallel Algorithms for Short-Range Molecular Dynamics. J Comput Phys 1995;117:1–19. https://doi.org/10.1006/jcph.1995.1039.

[57] Subramaniyan AK, Sun CT. Continuum interpretation of virial stress in molecular simulations. Int J Solids Struct 2008;45:4340–6. https://doi.org/10.1016/j.ijsolstr.2008.03.016.

[58] Marsh GE. THE VIRIAL THEOREM. Force-Free Magn. Fields Solut. Topol. Appl., vol. L, WORLD SCIENTIFIC; 1996, p. 9–16. https://doi.org/10.1142/9789812830524_0002.

[59] Chen W, Fish J. A mathematical homogenization perspective of virial stress. Int J Numer Methods Eng 2006;67:189–207. https://doi.org/10.1002/nme.1622.

[60] Stuart SJ, Tutein AB, Harrison JA. A reactive potential for hydrocarbons with intermolecular interactions. J Chem Phys 2000;112:6472–86. https://doi.org/10.1063/1.481208.

[61] Dilrukshi KGS, Dewapriya MAN, Puswewala UGA. Size dependency and potential field influence on deriving mechanical properties of carbon nanotubes using molecular dynamics. Theor Appl Mech Lett 2015;5:167–72. https://doi.org/10.1016/j.taml.2015.05.005.

[62] Mortazavi B. Ultrahigh thermal conductivity and strength in direct-gap semiconducting graphene-like BC6N: A first-principles and classical investigation. Carbon N Y 2021. https://doi.org/10.1016/j.carbon.2021.06.038.

[63] Edwards PM. Origin 7.0: Scientific graphing and data analysis software. J Chem Inf Comput Sci 2002;42:1270. https://doi.org/10.1021/ci0255432.

[64] Liu F, Ming P, Li J. Ab initio calculation of ideal strength and phonon instability of graphene under tension. Phys Rev B - Condens Matter Mater Phys 2007. https://doi.org/10.1103/PhysRevB.76.064120.

[65] Murali P, Guo TF, Zhang YW, Narasimhan R, Li Y, Gao HJ. Atomic Scale Fluctuations Govern Brittle Fracture and Cavitation Behavior in Metallic Glasses. Phys Rev Lett 2011;107:215501. https://doi.org/10.1103/PhysRevLett.107.215501.

[66] Mortazavi B, Shojaei F, Shahrokhi M, Azizi M, Rabczuk T, Shapeev A V., et al. Nanoporous C3N4, C3N5 and C3N6 nanosheets; novel strong semiconductors with low thermal conductivities and appealing optical/electronic properties. Carbon N Y 2020;167:40–50. https://doi.org/10.1016/j.carbon.2020.05.105.

[67] Mortazavi B, Lherbier A, Fan Z, Harju A, Rabczuk T, Charlier J-C. Thermal and electronic transport characteristics of highly stretchable graphene kirigami. Nanoscale 2017;9:16329–41. https://doi.org/10.1039/C7NR05231F.

[68] Parnell AJ, Dunbar ADF, Pearson AJ, Staniec PA, Dennison AJC, Hamamatsu H, et al. Depletion of PCBM at the Cathode Interface in P3HT/PCBM Thin Films as Quantified via Neutron Reflectivity Measurements. Adv Mater 2010;22:2444–7. https://doi.org/10.1002/adma.200903971.

[69] Prosa TJ, Winokur MJ, Moulton J, Smith P, Heeger AJ. X-ray structural studies of poly(3-alkylthiophenes): an example of an inverse comb. Macromolecules 1992;25:4364–72. https://doi.org/10.1021/ma00043a019.

[70] Savagatrup S, Makaram AS, Burke DJ, Lipomi DJ. Mechanical Properties of Conjugated Polymers and Polymer-Fullerene Composites as a Function of Molecular Structure 2014:1169–81. https://doi.org/10.1002/adfm.201302646.

[71] Yuan Z, Lu Z, Yang Z, Sun J, Xie F. A criterion for the normal properties of graphene/polymer interface. Comput Mater Sci 2016;120:13–20. https://doi.org/10.1016/j.commatsci.2016.04.006.

[72] Young RJ, Gong L, Kinloch IA, Riaz I, Jalil R, Novoselov KS. Strain Mapping in a Graphene Monolayer Nanocomposite

2011. https://doi.org/10.1021/nn2002079.

[73]   Compton OC, Cranford SW, Putz KW, An Z, Brinson LC, Buehler MJ, et al. Tuning the mechanical properties of graphene oxide paper and its associated polymer nanocomposites by controlling cooperative intersheet hydrogen bonding. ACS Nano 2012. https://doi.org/10.1021/nn202928w.

[74]   Keten S, Xu Z, Ihle B, Buehler MJ. Nanoconfinement controls stiffness, strength and mechanical toughness of B-sheet crystals in silk. Nat Mater 2010. https://doi.org/10.1038/nmat2704.

[75]   Oh JY, Rondeau-Gagné S, Chiu YC, Chortos A, Lissel F, Wang GJN, et al. Intrinsically stretchable and healable semiconducting polymer for organic transistors. Nature 2016. https://doi.org/10.1038/nature20102.

[76]   Zhang Y, Zhuang X, Muthu J, Mabrouki T, Fontaine M, Gong Y, et al. Load transfer of graphene/carbon nanotube/polyethylene hybrid nanocomposite by molecular dynamics simulation. Compos Part B Eng 2014;63:27–33. https://doi.org/10.1016/j.compositesb.2014.03.009.

Appendix A

A.1 Atomic structures in VASP POSCAR format

```
   C2N
   1.00000000000000
       7.2122787252451390     -4.1640110634861207      0.0000000000000000
       7.2122787252451390      4.1640110634861207      0.0000000000000000
       0.0000000000000000      0.0000000000000000     20.0000000000000000
     C     N
    12     6
Direct
   0.1585144514965240   0.5065441240447873   0.5000000032446579
   0.5065443472121564   0.3349414132998211   0.5000000133796121
   0.3349415042321459   0.5065442014302383   0.4999999981288852
   0.5065441836984880   0.1585144336647649   0.4999999972547187
   0.6650585109399240   0.4934557723764351   0.4999999958273094
   0.4934556638734969   0.6650585684882723   0.4999999896972582
   0.4934558053389176   0.8414855776060275   0.5000000026910740
   0.6650585937371739   0.8414855728507487   0.5000000070883672
   0.1585144057044890   0.3349413817177455   0.4999999962799464
   0.8414855424855912   0.4934558828637344   0.5000000069663599
   0.8414855883913699   0.6650586317635382   0.5000000034895535
   0.3349413942806952   0.1585144465692015   0.4999999968041493
   0.6689127688434986   0.9999999432511189   0.4999999934304284
   0.3310872196532196   0.0000000729107441   0.5000000036159662
   0.9999999934235007   0.6689127851312484   0.5000000128539668
   0.0000000029769964   0.3310872269992793   0.4999999898107390
   0.3310867460624885   0.6689131851779428   0.4999999846332770
   0.6689132776493316   0.3310867798543449   0.5000000048037094

   C3N
   1.00000000000000
       4.8602679153585626      0.0000000000000000      0.0000000000000000
      -2.4301339576792813      4.2091154839193639      0.0000000000000000
       0.0000000000000000      0.0000000000000000     15.0000000000000000
     C     N
     6     2
Direct
   0.3334032823986632   0.1667016411993245   0.5000000000000000
   0.1667016411993245   0.3334032823986632   0.5000000000000000
   0.8332983588006755   0.1667016411993245   0.5000000000000000
   0.1667016411993245   0.8332983588006755   0.5000000000000000
   0.8332983588006755   0.6665967176013368   0.5000000000000000
   0.6665967176013368   0.8332983588006755   0.5000000000000000
   0.6666666666666643   0.3333333333333357   0.5000000000000000
   0.3333333333333357   0.6666666666666643   0.5000000000000000

   C3N4
   1.00000000000000
   4.7842289992586231 0.0000000000000000 0.0000000000000000
```

```
1    -2.3921145001293280 4.1432638514578919 0.0000000000000000
2    0.0000000000000000 0.0000000000000000 15.0000000000000000
3    C    N
4    3    4
5    Direct
6    0.4901791484096898 0.9803579955387230 0.500000007464354
7    0.0196423692683693 0.5098211057673385 0.500000000241522
8    0.4901795040440148 0.5098202626505081 0.500000011373595
9    0.1701263316295368 0.8298738856915344 0.500000023163407
10   0.1701265063818060 0.3402525198699708 0.4999999936372895
11   0.6597470668246924 0.8298731718163589 0.4999999989302001
12   0.6666670734418921 0.3333330586655647 0.500000032082155
13
14      C6N6
15      1.00000000000000
16        7.1191481771357914      0.0000000000000000      0.0000000000000000
17        3.5595195379452571      6.1652239484675073      0.0000000000000000
18        0.0000000000000000      0.0000000000000000     15.0000000000000000
19      C    N
20      6    6
21   Direct
22    0.1224025602763277  0.4388012633542004  0.5000000000000000
23    0.4387997278595037  0.1224022332359667  0.5000000000000000
24    0.4387981643816161  0.4388014840569099  0.5000000000000000
25    0.5612018066183779  0.5611985459430855  0.5000000000000000
26    0.5612003021404917  0.8775977597640363  0.5000000000000000
27    0.8775974467236765  0.5611987366457996  0.5000000000000000
28    0.4434438088949904  0.7782783199922321  0.5000000000000000
29    0.7782791996757155  0.4434389630393269  0.5000000000000000
30    0.7782757114588108  0.7782786379211331  0.5000000000000000
31    0.2217242745411951  0.2217213620788669  0.5000000000000000
32    0.2217207853242869  0.5565610079606671  0.5000000000000000
33    0.5565561611050001  0.2217216800077750  0.5000000000000000
34
35      C7N6
36      1.00000000000000
37        6.7943948564804693      0.0000000000000000      0.0000000000000000
38        3.3971974282402351      5.8841185491832784      0.0000000000000000
39        0.0000000000000000      0.0000000000000000     15.0000000000000000
40      C    N
41      7    6
42   Direct
43    0.9998100576047193  0.0002509396813224  0.5000000000000000
44    0.9331640163519950  0.7159702217766863  0.5000000000000000
45    0.9331204068991781  0.3511955830278453  0.5000000000000000
46    0.7155979589857679  0.9335029314294445  0.5000000000000000
47    0.7155586812735208  0.3512017827147176  0.5000000000000000
48    0.3507638336030467  0.9335002995972488  0.5000000000000000
49    0.3507380370779813  0.7159747027046279  0.5000000000000000
50    0.1110737155275103  0.1115015469972604  0.5000000000000000
```

1	0.1110716970172021	0.7777302000807538	0.5000000000000000
2	0.9928516147958462	0.5037223459642206	0.5000000000000000
3	0.7772919263856721	0.1115054214509428	0.5000000000000000
4	0.5034145543584359	0.9930456207717029	0.5000000000000000

5

Appendix B

B.1 Composite elastic modulus tested with strain rate 2.0x10⁹s⁻¹ at 300K; the unit is regarded as GPa.

B.1 Composite elastic modulus tested with strain rate $2.0 \times 10^9 s^{-1}$ at 300K; the unit is regarded as GPa.

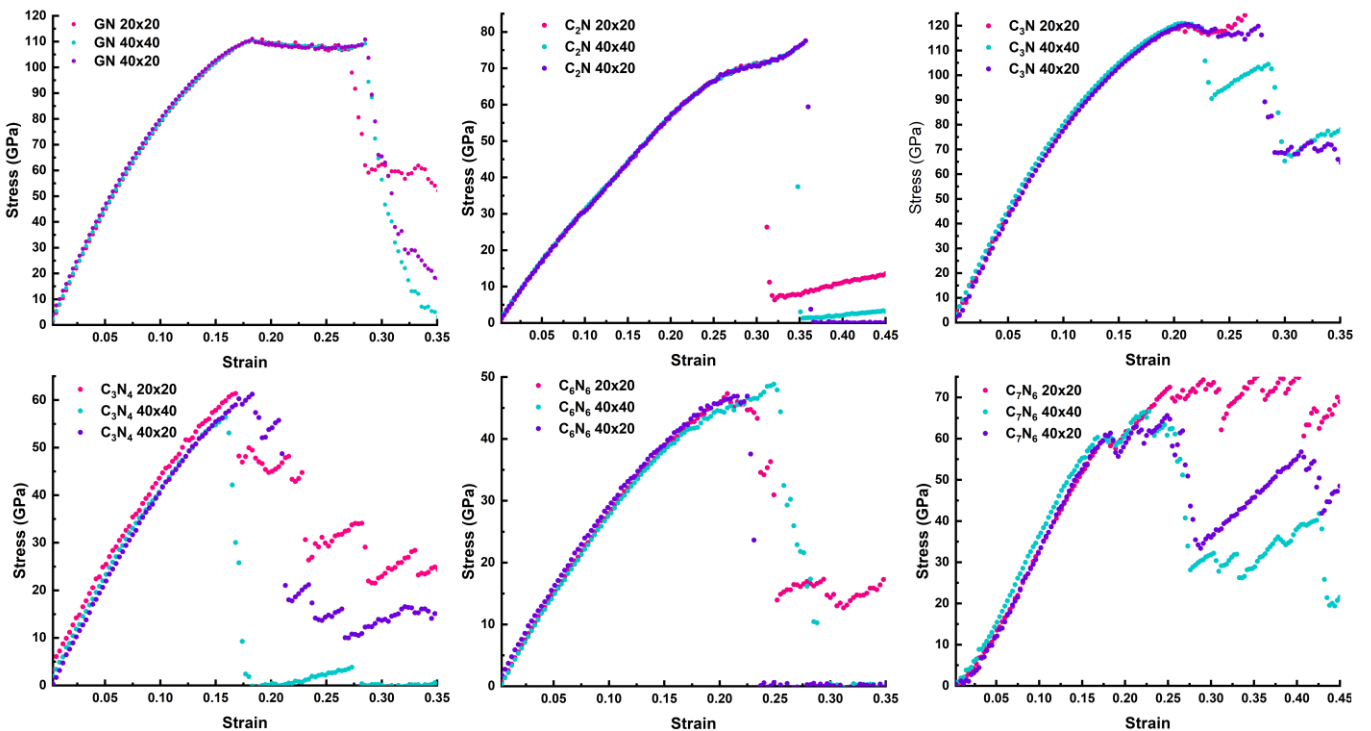| Volume fractions	5%	10%	15%
C_2N/P3HT	3.103	2.810	2.469
C_3N/P3HT	2.320	1.629	2.164
C_3N_4/P3HT	1.806	2.209	2.187
C_6N_6/P3HT	1.657	2.861	2.606
C_7N_6/P3HT	2.257	2.476	1.968
Graphene/P3HT	1.579	3.237	3.386

B.2 Reinforced composite elastic modulus enhancement comparing with pure P3HT matrix.

Volume fractions	5%	10%	15%
C_2N/P3HT	0.45	2.05	2.11
C_3N/P3HT	1.85	1.58	0.49
C_3N_4/P3HT	1.13	0.49	0.99
C_6N_6/P3HT	0.66	1.03	1.01
C_7N_6/P3HT	0.52	1.62	1.39
Graphene/P3HT	1.07	1.27	0.81

Appendix C

C.1 The size effect test of Graphene and C_xN_y nanosheet with width and height (20x20, 40x40, 40x20 Å), with a strain rate of $6.0 \times 10^9 s^{-1}$.

The target reinforcement size mainly comes from the extending of a single lattice by 5x5 in the X and Y-direction. To keep the integrity of the lattice and the adaptability among different C_xN_y, around 40x20 Å reinforcement size was chosen. The test shows that the size effect influence for 20x20, 40x40, 40x20 Å in X-direction loading is so small. That means the choice of such a size will not influence much for the mechanical properties of the monolayer. Moreover, while cutting the lattice to achieve target size, if the lattice integrity can be kept well, then the mechanical properties will not be influenced much by size. Otherwise, the mechanical properties will decrease due to destroying the lattice.